

The Carnegie-Chicago Hubble Program. IX. Calibration of the Tip of the Red Giant Branch Method in the Mega-Maser Host Galaxy, NGC 4258 (M106)*

In Sung Jang,^{1,2} Taylor Hoyt,² Rachael Beaton,^{3,4} Wendy L. Freedman,² Barry F. Madore,^{4,2}
Myung Gyoon Lee,⁵ Jillian R. Neeley,⁶ Andrew J. Monson,⁷ Jeffrey A. Rich,⁴ AND Mark Seibert⁸

¹Leibniz-Institut für Astrophysik Potsdam (AIP), An der Sternwarte 16, 14482 Potsdam, Germany

²Dept. of Astronomy & Astrophysics, Univ. Chicago, 5640 S. Ellis Ave., Chicago, IL, 60637

³Dept. of Astrophysical Sciences, Princeton University, 4 Ivy Lane, Princeton, NJ 08544

⁴The Observatories, Carnegie Institution for Science, 813 Santa Barbara St., Pasadena, CA 91101

⁵Department of Physics & Astronomy, Seoul National University, Gwanak-gu, Seoul 151-742, Republic of Korea

⁶Department of Physics, Florida Atlantic University, 777 Glades Rd., Boca Raton, FL 33431, USA

⁷Department of Astronomy & Astrophysics, The Pennsylvania State University, 525 Davey Lab, University Park, PA 16802, USA

⁸Unaffiliated, Pasadena, CA 91101, USA

ABSTRACT

In the nearby galaxy NGC 4258, the well-modeled orbital motion of H₂O masers about its super-massive black hole provides the means to measure a precise geometric distance. As a result, NGC 4258 is one of a few “geometric anchors” available to calibrate the true luminosities of stellar distance indicators such as the Tip of the Red Giant Branch (TRGB) or the Cepheid Leavitt law. In this paper, we present a detailed study of the apparent magnitude of the TRGB within NGC 4258 using publicly-available *HST* observations optimally situated in the unreddened stellar halo along the minor axis, spanning distances ranging from 8 to 22 kpc in projected galactocentric radius, or 6′ (13 kpc) to 30′ (66 kpc) in distance along the semi-major axis. We undertake a systematic evaluation of the uncertainties associated with measuring the TRGB in this galaxy, based on an analysis of 54 arcmin² of HST/ACS imaging. After quantifying these uncertainties, we measure the TRGB in NGC 4258 to be $F814W_0 = 25.347 \pm 0.014$ (stat) ± 0.042 (sys) mag. Combined with a recent 1.5% megamaser distance to NGC 4258, we determine the absolute luminosity of the TRGB to be $M_{F814W}^{\text{TRGB}} = -4.050 \pm 0.028$ (stat) ± 0.048 (sys) mag. This new calibration agrees to better than 1% with an independent calibration presented in Freedman et al. (2019, 2020) that was based on detached eclipsing binaries (DEBs) located in the LMC.

Keywords: distance scale — stars: Population II — galaxies: individual (NGC4258) — galaxies: stellar content — galaxies: structure

1. INTRODUCTION

There have been major advances in our ability to measure cosmological parameters to high precision and accuracy over the past two decades (e.g., Freedman & Turner

2003, and references therein for an early review). Effectively unchanged, however, is the role of the Hubble Constant (H_0) in framing our current cosmological understanding. Early universe and local distance-scale methods appear to disagree at a significant level, causing concern that our cosmological model may require revision (see, e.g., Freedman 2017; Verde et al. 2019, and references therein). An equally valid interpretation of our current H_0 -tension is that the quoted uncertainties have been underestimated, not due to a lack of rigor in analyses, *per se*, but rather because not all sources of systematic uncertainty have yet been identified, as the

Corresponding author: In Sung Jang
hanlbomi@gmail.com

* Based on observations made with the NASA/ESA Hubble Space Telescope, obtained at the Space Telescope Science Institute, which is operated by the Association of Universities for Research in Astronomy, Inc., under NASA contract NAS 5-26555. These observations are associated with programs GO-9477 and GO-10399

quoted uncertainties have decreased from the 10% to the 1% level over the last two decades.

The nearby spiral galaxy, NGC 4258 plays a significant role in establishing the absolute calibration of the modern distance scale. At a distance of 7.58 Mpc (Reid et al. 2019), NGC 4258 is the closest galaxy, beyond the Local Group, with a geometric distance measurement; and, it is still sufficiently nearby that detailed studies of its resolved stellar populations can be made by currently-operating, space-based telescopes. The next closest megamaser host galaxy is UGC 3789, at a distance of $D = 51.5^{+4.5}_{-4.0}$ Mpc or $\mu = 33.6^{+0.19}_{-0.17}$ mag (Pesce et al. 2020). The data analysis techniques employed in determining the megamaser-based distances are both elegant and complex (for example, see *The Introduction to the Megamaser Cosmology Project*, Reid et al. 2009). Once the maser distance is secured, other (more widely applicable) distance indicators that have also been studied in NGC 4258, such as the TRGB stars and Cepheids, can have their zero points accurately established.

In addition to playing an important role in the distance ladder, NGC 4258 has been included in several large-scale galaxy evolution programs that have provided a rich set of multi-wavelength datasets (Heald et al. 2011; Kim et al. 2011; Spencer et al. 2014; Merritt et al. 2016; Sabbi et al. 2018). Thus, there is a wealth of archival data on this galaxy, much of it yet to be exploited for the purposes of calibrating the extragalactic distance scale. Here we tap into that reservoir of data, specifically in the context of calibrating the TRGB method.

In the following, we use *HST* imaging of NGC 4258 as a means of identifying and quantifying the uncertainties associated with TRGB measurements. In the process, we provide a high-confidence TRGB measurement in NGC 4258 and rigorously quantify the associated systematic and statistical uncertainties.

This paper is organized as follows: First in section 2, we describe the *HST* imaging datasets that we have analyzed, describe the image processing undertaken, followed by an account of stellar photometry methods used and their calibration. In section 3, we present a detailed comparison of two independent photometry analyses (using DOLPHOT and DAOPHOT), allowing us to examine the impact of differences in adopted input parameters. In section 4, we present the CCHP TRGB measurement, followed in section 5 by a discussion of previously published measurements. Calibration of the TRGB using the maser distance is presented in section 6. The results of the paper are summarized in section 7. Finally, in a set of appendices, we discuss the photometric accuracy with the choice of sky fitting algorithms (Ap-

pendix A), stellar-population variations and their potential impact (Appendix B), and provide an independent analysis of earlier WFPC2 data (Appendix C).

2. DATA AND DATA PROCESSING

2.1. Archival *HST* Data

Figure 1 presents the totality of mosaiced data used for this work as retrieved from the MAST archive, largely constructed from ACS observations obtained in parallel-mode. The upper left panel of Figure 1 is a color image of the contiguous area used for this work that has both F555W and F814W imaging to a sufficient depth for a TRGB analysis; red, green, and blue channels of the color image are taken from F814W, $(F555W - F814W)/2$, and F555W, respectively. The mosaic is made from 15 individual ACS pointings with details on the observations for each pointing provided in Table 1. As given in Table 1, the individual pointings span a region ranging from a galactocentric radius of 4.2 to 10.5 in projection from the center of NGC 4258. NGC 4258 has an inclination of $i = 68.3^\circ$ with a position angle of 150° (taken from HyperLeda¹; Makarov et al. 2014), such that our mosaic corresponds to a disk semi-major axis (SMA) ranging from 5.7 (13 kpc) to 31.1 (68 kpc).

The upper right panel of Figure 1 places this imaging in the context of the large-scale structure of NGC 4258, using a wide-field image taken with the *Dragonfly* array (Abraham & van Dokkum 2014; Merritt et al. 2016), which is constructed from the g and r -band image data with r for red, g for green, and $2 \times g - r$ for blue. The region we use is outlined in yellow and is more-or-less on the minor axis of NGC 4258; the majority of its area is beyond a de-projected semi-major axis (SMA) of $14'$, corresponding to a physical radius in the NGC 4258-disk of approximately 30 kpc. The blue outlined region (to the lower left) interior to $SMA = 14'$ is the ACS pointing that has been used in prior work to measure the TRGB (e.g. Macri et al. 2006; Rizzi et al. 2007; Reid et al. 2019) that we will refer to as the Disk pointing.

Recent work in the Milky Way has used chemodynamical evidence to identify disk-like stars as far as $R_{\text{Gal}} = 24$ kpc, while also finding stars with disk-like chemistry at significant vertical scale heights (Hayes et al. 2018, and references therein). Thus, we anticipate that our innermost regions may be contaminated by stellar populations belonging to the outer disk of NGC 4258, while our outermost regions are expected to have significantly less disk contamination.

¹ <http://leda.univ-lyon1.fr/>

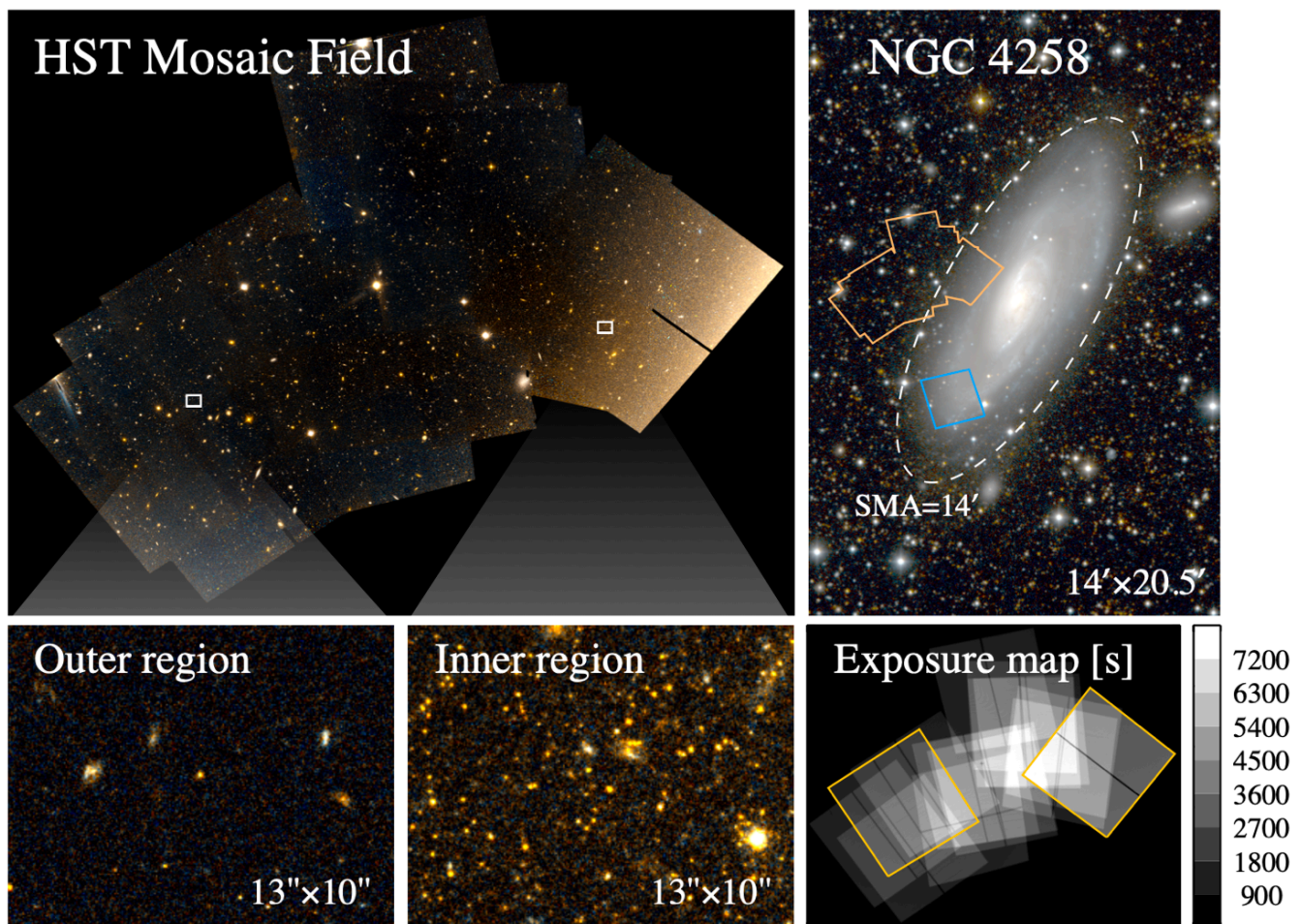


Figure 1. Summary of the *HST* imaging data for NGC 4258 used in this study. Top left: The full mosaic of 15 individual *HST*/ACS fields. The area of the mosaic is 54 arcmin^2 , approximately five times larger than a single ACS field, and spans from $SMA = 6'$ (13 kpc) to $30'$ (66 kpc) from the center of NGC 4258. Top right: identification of the *HST*/ACS fields used in this and previous studies overlaid on an image taken with the Dragonfly array (Abraham & van Dokkum 2014). The mosaic ACS field (orange polygon) lies on the minor axis of the galaxy and a single field (blue square) in the disk of the galaxy indicates observations taken for the analysis of Cepheid variables, which we later use for comparison with the halo mosaic dataset. We use the region beyond $SMA = 14'$ to define a selection of halo member stars. Bottom: zoom-in views of the outer (left) and inner (middle) regions of the mosaic ACS field. The exposure weight map in *F814W* is shown in the last panel. Yellow squares indicate Field 1 (right) and Field 13 (left) we used for a photometry comparison. North is up and east is to the left in all the panels.

The lower left panels of Figure 1 give a sense of how the source density varies across the region, by providing zooms into two locations of the mosaic that are representative of lower stellar density (outer region) and higher stellar density (inner region). As is visually apparent in these panels, the region spans a large range of on-sky source densities. The inclusion of high-density regions in our image footprint is intentional; these regions allow us to study explicitly how source density, and variations in the underlying stellar populations, impact measurements of the TRGB.

Lastly, the lower right panel of Figure 1 provides the exposure map of the image mosaic for the *F814W* filter.

In the mosaic, the median exposure time is 2,780 sec with a standard deviation of 1,770 sec; the maximum exposure time is 10,460 sec. Using prior work as a guide, the magnitude of the TRGB is expected to be around $F814W = 25.3\text{--}25.4 \text{ mag}$ (e.g., Jang & Lee 2017); the median exposure time predicts a signal-to-noise of 17.1 to 18.6 at this magnitude, enabling the detection and measurement of the TRGB across the full extent of the mosaic.

2.2. Photometry

The first step in our analysis is the construction of a photometric catalog of the resolved stars in the halo of NGC 4258. We now briefly describe that process.

Table 1. Archival *HST/ACS* Images used in This Study

Field	R.A.	Decl.	R	SMA^a	Exposure Time(s)		Obs. date	Zero-points ^c		Prop. ID
	(2000.0)	(2000.0)	[arcmin]	[arcmin (kpc) ^b]	$F555W$	$F814W$		$F555W$	$F814W$	
F1	12:19:18.31	47:20:09.8	4.2	11.0 (24.3)	5700	2600	2003-05-05	25.736	25.531	9477
F2	12:19:25.32	47:20:32.3	5.3	14.1 (31.1)	900	900	2005-07-30	25.731	25.528	10399
F3	12:19:26.11	47:20:11.5	5.3	14.0 (30.8)	900	900	2005-07-24	25.731	25.528	10399
F4	12:19:31.26	47:21:10.9	6.5	17.3 (38.2)	900	900	2005-07-08	25.731	25.528	10399
F5	12:19:32.63	47:21:06.7	6.7	17.8 (39.2)	900	900	2005-07-11	25.731	25.528	10399
F6	12:19:33.13	47:21:36.3	7.0	18.7 (41.1)	900	900	2005-07-15	25.731	25.528	10399
F7	12:19:38.43	47:22:22.0	8.2	21.8 (48.1)	900	900	2005-07-01	25.731	25.528	10399
F8	12:19:38.50	47:19:30.5	7.1	18.1 (39.9)	900	900	2005-07-02	25.731	25.528	10399
F9	12:19:38.73	47:19:17.7	7.1	18.0 (39.6)	900	900	2005-06-29	25.731	25.528	10399
F10	12:19:41.91	47:19:25.9	7.7	19.4 (42.8)	900	900	2005-07-02	25.731	25.528	10399
F11	12:19:42.48	47:18:30.1	7.7	18.7 (41.3)	900	900	2005-04-02	25.732	25.528	10399
F12	12:19:51.59	47:19:30.6	9.3	23.5 (51.8)	900	900	2005-06-01	25.731	25.528	10399
F13	12:19:55.78	47:18:56.7	10.0	24.5 (54.0)	900	900	2005-06-02	25.731	25.528	10399
F14	12:19:53.91	47:17:33.7	9.6	22.2 (48.9)	900	900	2005-05-28	25.732	25.528	10399
F15	12:19:59.20	47:18:00.5	10.5	24.8 (54.7)	900	900	2005-05-25	25.732	25.528	10399

^aSemi-Major Axis of the stellar disk that has a position angle of 150° and an inclination angle of 68.3° (HyperLeda).

^bAssuming the distance of $D=7.58$ Mpc from Reid et al. (2019).

^cFrom the ACS zero-point calculator (<https://acszeropoints.stsci.edu/>).

In this study, we have undertaken the bulk of the photometric reductions using DOLPHOT (Dolphin 2000), as it has distortion correction routines for the HST instruments that are not available within our existing DAOPHOT pipeline. The archival imaging data for NGC 4258 have large offsets with different orientation angles between the fields and were not taken with a standard dither pattern, as for our CCHP program. One of the main difficulties encountered in the NGC 4258 data reduction involved the alignment and registration of the individual FLC images, each of which has strong geometric distortions known to be generated by the camera optics.

The CCHP has developed its own point-spread-function (PSF) fitting photometry pipeline that is based on DAOPHOT (Stetson 1987) and models synthetic PSFs from TinyTim (Krist et al. 2011). The most detailed description of the pipeline is given in Beaton et al. (2019) and the pipeline is specifically designed to provide robust, homogenous measurements of resolved stars in HST images. It has been used to measure TRGB distances to nearby SN Ia host galaxies (Hoyt et al. 2019; Freedman et al. 2019; Beaton et al. 2019). The CCHP pipeline was designed around single fields and not multiple fields with differing orientations, as can be seen

in Figure 1. While the pipeline could be adapted, we found the native tools of DOLPHOT better adapted to the task. With these caveats between the two reduction packages noted, we performed extensive tests to search for and quantify differences between the methodologies used in this paper and the CCHP pipeline results.

We developed an independent photometry pipeline based on DOLPHOT to perform simultaneous photometry on all the individual image frames associated with the mosaic data of NGC 4258. We have also reduced the data for a subset of the fields using DAOPHOT. This approach provides a unique opportunity to check the robustness of our photometry specifically with respect to the choice of software, as discussed in detail in subsection 3.1.

DOLPHOT uses the WCS information contained in image headers to obtain an initial alignment solution. We inspected the header WCS entries to see whether the images were properly aligned, and found that some image frames showed visible offsets of up to $2''$ with respect to others. Such WCS-offsets are naturally expected for images taken from different visits that use different guide stars for alignment. We thus aligned images by updating the header WCS information using the

DrizzlePac.TweakReg task (Gonzaga & et al. 2012) as follows.

The TweakReg task in DrizzlePac provides an automated interface for detecting sources and using them to compute the shifts between the input images. We initially applied this task to the original WCS in the FLC images, but found that the resulting alignment solution was not sufficient to get robust photometry. We suspect that this uncertainty is most likely driven by the lack of bright stellar sources in the images for two reasons: NGC 4258 is located at a high galactic latitude ($b \sim 68.8$ deg) and the target field is sampling the low-surface brightness (halo) regions of the galaxy. In this situation, the DrizzlePac manual suggests using a list of reliable sources manually selected from initial photometry from DAOPHOT or SExtractor; thus, we carried out preliminary PSF photometry on the FLC images using DAOPHOT to construct just such a list of bright sources.

At this stage, the source list contained a large number of cosmic rays or other defects, in addition to genuine astronomical objects (stars & background galaxies). To reduce the non-astronomical contamination, we matched pairs of source lists for co-spatial regions in the WCS domain with a matching tolerance of 1 pixel ($0''.05$). With the source lists cleaned, TweakReg task found a better alignment solution with a typical *rms* value of 0.1 pixels ($0''.005$). The well-aligned FLC images were then used to make a stacked drizzled frame with the AstroDrizzle task. DrizzlePac also updates the data quality (DQ) extension of FLC images by providing pixel-level flags identifying cosmic rays and hot pixels. Finally, we repeated the steps from our preliminary PSF photometry, this time using cosmic-ray-masked FLC images to again improve the alignment solution.

A standard sequencing of the DOLPHOT procedures for the ACS module was then executed: *acsmask* - *splitgroups* - *calcsky* - *dolphot*. A total 120 FLC images were simultaneously photometered with the TinyTim PSFs implemented within DOLPHOT. We used the drizzled mosaic frame in the F814W-band to coordinate the reference source positions. For *calcsky*, we used the values recommended in the manual: $r_{in} = 15$, $r_{out} = 35$, $step = 4$, $\sigma_{low} = 2.25$, and $\sigma_{high} = 2.00$. A list of input parameters we used for the DOLPHOT task is summarized in Table 2. These parameters are broadly consistent with the recommended values in the manual, but there are slight changes. For example, we set **Align** = 4 with **UseWCS** = 1 to achieve a more elaborate geometric distortion correction using a full third-order polynomial fit. The **FitSky** parameter determines the algorithm used for the local background estimation. Following the

photometry processing in the PHAT survey (Dalcanton et al. 2012), we adopted **FitSky** = 3, which fits simultaneously the sky background and the PSF within the fitting radius. Most importantly, we set **ApCor** = 0, which means that we did not apply the aperture corrections automatically determined from the code itself; instead we examined bright stars and determined the correction values manually. The details of our manually-derived aperture correction are given in the next section.

We later explore the robustness of our photometry by varying several key parameters (**RPSF**, **FitSky**, and **ACSpsfType**) in section 3. From these analyses, we find that the systematic error associated with the choice of photometry parameters is at most 0.01 mag.

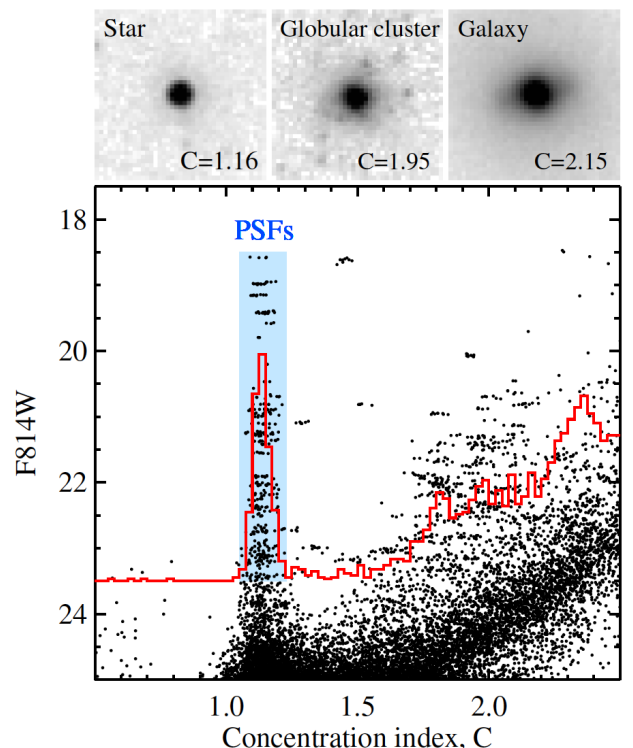


Figure 2. Selection of high-quality point sources for the aperture correction. The *Concentration Index*, C , the difference in magnitude measured with small and large aperture radii, more specifically: $C = \text{mag}(r = 0.8 \text{ pix}) - \text{mag}(r = 2.5 \text{ pix})$. A strong plume of point sources is seen at $C \sim 1.1$. Overlaid in red is a histogram for the sources brighter than $F814W = 23.5$ mag, showing the steep rise of sources at larger C . The upper three panels (from left to right) show the F814W-band thumbnail images ($2'' \times 2''$) for a stellar point source, a globular cluster, and a background galaxy, with their C values in F814W marked at the bottom of each image. These selection criteria were only applied for the determination of aperture corrections.

2.3. Aperture Correction and Photometry Calibration

Table 2. DOLPHOT Processing Parameters

Description	Parameter	Value
Inner and outer sky radii	img_apsky	15 25
Photometry aperture size	img_RAper	8
χ -statistic aperture size	img_RChi	2
Photometry type	PSFPhot	1
Fit sky?	FitSky	3
PSF size	img_RPSF	13
Spacing for sky measurement	SkipSky	2
Sigma clipping for sky	SkySig	2.25
Second pass finding stars	SecondPass	5
Searching algorithm	SearchMode	1
Sigma detection threshold	SigFind	2.5
Multiple for quick-and-dirty photometry	SigFindMult	0.85
Sigma output threshold	SigFinal	3.5
Maximum iterations	MaxIT	25
Noise multiple in imgadd	NoiseMult	0.10
Fraction of saturate limit	FSat	0.999
Find/make aperture corrections?	ApCor	0
Force type 1/2?	Force1	0
Use WCS for initial alignment?	useWCS	1
Align images?	Align	4
Allow cross terms in alignment?	Rotate	1
Centroid box size	RCentroid	2
Search step for position iterations	PosStep	0.25
Maximum single step in position iterations	dPosMax	3.0
Minimum separation for two stars for cleaning	RCombine	1.415
Minimum S/N for PSF parameter fits	SigPSF	3.0
Make PSF residual image?	PSFres	1
Coordinate offset	psfoff	0.0
Use saturated cores?	FlagMask	4
Use the DOLPHOT CTE correction	ACSuseCTE	0
PSF Type	ACSpsfType	0

The approximate nature of PSF photometry, together with the finite size of the radius used by crowded-field photometry applications, requires an additional term for calibration, commonly known as the ‘aperture correction’. This term corrects for the difference between the measured flux at finite radius and the total stellar flux, as measured at infinity. As previously described, we performed PSF photometry on our dataset, and so the infinite aperture correction step is divided into two distinct steps: a correction from PSF to aperture magnitudes at finite radius, and a correction from the finite radius aperture to infinity. The latter is provided for ACS by STScI, so the bulk of this section covers the former, namely our

empirical determination of the transformation from the PSF to an aperture magnitude system at finite radius.

DOLPHOT provides a routine for the aperture correction by setting `ApCor = 1`. This routine selects bright stars in the individual frame images and calculates the necessary correction. This option can be convenient in generic cases, however it can be difficult to know exactly what goes into the automated process, and for the high precision, high accuracy photometry demanded by the extragalactic distance scale, we prefer to directly measure the aperture corrections outside of DOLPHOT. Accordingly, we independently measured the aperture cor-

rection (with $\text{ApCor} = 0$) by first manually examining reliable point sources.

We selected the bright point sources based on the concentration parameter, C , which is the difference between magnitudes measured with small and large aperture radii: $C = \text{mag}(r = 0.8 \text{ pix}) - \text{mag}(r = 2.5 \text{ pix})$. Figure 2 shows our selection criteria for these bright point sources. The C values are derived from the aperture photometry on individual FLC images, after the cosmic ray masking. We plotted the values taken from all the images together in Figure 2. Because we have 120 FLC images in the mosaic field, some stars were multiply imaged onto different positions on the detector and independently photometered. We expect intrinsic scatter in the C values, as the PSF is known to vary across the HST focal plane. Nevertheless, the figure shows a strong plume of sources at $C \sim 1.1$, which are identified as *bona fide* point sources. In addition to the empirical determination of the point source sequence given above, we applied this same *Concentration Index* procedure to artificial point sources that were injected into several regions across the FLC images. We confirmed that the injected sources, and thus our PSF model, also has a mean C value of ~ 1.1 , consistent with that seen in the real data.

In the upper panels in Figure 2, we display thumbnail images of three representative types of sources taken from the stacked F814W frame: a star, a globular cluster candidate in the NGC 4258 halo², and a background galaxy. It is clear that the star ($C \sim 1.16$) is well separated from the other detected sources ($C \sim 1.95$ for the globular cluster candidate and $C \sim 2.15$ for the background galaxy), in both the *Concentration Index* and their morphology. We thus selected the bright point sources in the shaded region of the figure, and used them for the aperture correction after a careful visual inspection.

Using this list of bright and isolated point sources (standard stars), we computed growth curves for the standard stars contained in each FLC frame. We set 12 aperture radii to construct the growth curves out to 14 pixels ($0''.7$). For a small subset of the selected standard stars, the growth curves provided evidence that additional faint neighbor stars were contaminating the aperture. To correct for this contamination, and to measure the unbiased transformation from PSF to aperture magnitudes, we manually subtracted the neighbor

sources using the SUBSTAR task in DAOPHOT, and then re-computed the growth curves from the cleaned stellar profile. In Table 3, we provide the final list of stars used for the aperture corrections and the calibrated magnitudes we measure at a 5 pixel radius. Photometric zero-points are derived from the online STScI ACS Zeropoints Calculator³ as listed in Table 1. There are 64 and 38 standard stars distributed over the entire mosaic of the F814W and F555W fields, respectively. The mean photometric error of the standard stars is smaller than 0.01 mag in each filter.

From the growth curves, a correction from the PSF magnitudes to the $r = 5$ pixel aperture magnitudes was determined for each frame. We found that each F814W and F555W frame contains on average ~ 7 and ~ 4 standard stars, respectively. The statistical uncertainty for the aperture corrections is smaller than 0.01 mag for F814W and at the level of 0.01 mag for F555W. From this, we adopt 0.01 mag as a systematic uncertainty associated with the aperture correction. The mean correction for the 60 F814W (F555W) frames is 0.077 (0.089) mag with a standard deviation of 0.012 (0.019) mag. The calibrated magnitudes in each FLC frame were then combined in the flux domain, resulting in the deepest possible photometric catalog. With the PSF photometry now calibrated to a 5-pixel aperture, a correction from $r = 5$ pixel to infinity (Bohlin 2016) was applied: -0.1726 mag for F814W and -0.1537 mag for F555W (all data were obtained before the ACS servicing mission).

2.4. Artificial Star Tests

A robust determination of stellar flux and associated properties requires in-depth understanding of uncertainties. In crowded-field photometry, it is known that the error of stellar flux is not simply defined by purely Poisson statistics because unresolved sources below the detection limit will contribute to the main source flux, potentially resulting in a bias. There are three key indicators to assess the robustness of stellar photometry: statistical errors (precision), systematic errors (accuracy), and recovery rates (completeness). Estimating them using the real star photometry alone is very difficult (or near to impossible); rather a series of tests with artificial stars is needed. We thus carried out extensive artificial star tests on our photometry of NGC 4258.

We used DOLPHOT for the artificial star tests with the general procedures described in the DOLPHOT User's guide and, in particular, the manual provided by

² The position of the globular cluster candidate is RA = 12:19:25.89, and DEC = +47:22:55.5. It is $6''.72$ away from the center of NGC 4258 corresponding to a projected physical distance of 14.8 kpc at 7.58 Mpc (Reid et al. 2019).

³ <https://acszeropoints.stsci.edu/>

Table 3. A List of Bright and Isolated Stars used for the Aperture Correction

ID	R.A. (2000.0)	Decl. (2000.0)	F814W ($r = 5$ pix)	N(stdev) ^a	F555W ($r = 5$ pix)	N(stdev) ^a
1	12:19:08.518	47:19:52.95	22.396 ± 0.007	2(0.014)
2	12:19:08.558	47:20:09.50	19.797 ± 0.001	2(0.001)
3	12:19:08.580	47:19:46.43	23.096 ± 0.016	1	23.753 ± 0.013	1
4	12:19:09.346	47:20:05.46	22.926 ± 0.009	2(0.008)	22.997 ± 0.007	1
5	12:19:11.656	47:21:03.28	21.106 ± 0.004	1
6	12:19:11.741	47:20:25.83	22.682 ± 0.011	1
7	12:19:11.825	47:19:17.62	23.796 ± 0.013	1
8	12:19:12.235	47:18:51.94	22.706 ± 0.013	1
9	12:19:15.970	47:21:16.93	22.504 ± 0.005	5(0.019)
10	12:19:16.128	47:19:02.56	20.468 ± 0.002	2(0.000)	21.762 ± 0.004	1
11	12:19:17.761	47:19:23.40	23.100 ± 0.014	1
12	12:19:18.153	47:20:53.39	23.223 ± 0.015	1
13	12:19:18.318	47:22:00.09	23.411 ± 0.011	2(0.021)
14	12:19:18.933	47:18:12.73	22.960 ± 0.009	2(0.004)
15	12:19:20.303	47:18:19.42	20.490 ± 0.005	1
16	12:19:20.969	47:20:46.56	22.027 ± 0.007	4(0.024)	23.924 ± 0.012	1
17	12:19:21.504	47:19:27.83	21.904 ± 0.005	4(0.003)
18	12:19:22.507	47:21:36.83	22.758 ± 0.007	5(0.015)
19	12:19:22.991	47:20:20.11	23.530 ± 0.016	3(0.036)
20	12:19:22.994	47:20:20.05	22.367 ± 0.005	8(0.010)

^a The number of independent measurements from different FLC frames, and their standard deviation of the $r = 5$ pixel aperture magnitudes.

(This table is available in its entirety in machine-readable form.)

Bill Harris⁴. We generated artificial stars with a wide range in color ($-1 < (F555W - F814W) < 4$ mag) and in magnitude ($22 < F814W < 28$ mag) to span the color-magnitude range shown in Figure 3(a). The spatial distribution of the input stars was based on the distribution of real stars, placing more stars in the inner high-surface brightness regions (Figure 3(a) inset). About 350,000 artificial stars were injected into each image and recovered alongside the real stars using the identical procedures as adopted to derive the primary catalog. Because DOLPHOT performs the test in a star-by-star manner, the intrinsic degree of stellar crowding local to the artificial star is not significantly impacted by this process.

The results of the artificial star tests are shown in Figure 3. Figure 3(a) displays the recovery rate in color-magnitude space compared to stellar isochrones from PARSEC (Bressan et al. 2012). Figure 3(b) displays the recovery fraction of the artificial stars with $1.0 < F555W - F814W < 2.0$, as a function of input F814W magnitude ($F814W_{in}$) for the full mosaic (solid black) and the regions interior to (red dashed) and ex-

terior to (blue dotted) SMA=14'. The recovered stars have passed the point source selection criteria that we shall explain in the next section. We found that our photometry is complete enough to detect the NGC 4258 TRGB: the recovery fractions are higher than 90% at the anticipated TRGB at $F814W \sim 25.4$ mag. The fractions are still as high as 80% at approximately 1 mag fainter than the TRGB. We also found that there is a difference in completeness depending on the spatial selection. For faint sources (with $F814W \gtrsim 26.5$ mag), the inner crowded region (SMA < 14') shows higher recovery fractions than the outer region (SMA > 14'). We infer that this is likely due to the difference in the effective exposure time, as the inner SMA < 14' region has a longer median exposure time ($F814W = 3017$ s and $F555W = 6165$ s) than the outer region ($F814W = 2736$ s and $F555W = 2742$ s). By contrast, for brighter sources ($24 \lesssim F814W \lesssim 26$ mag), the trend reverses, suggesting that crowding effects, due to higher source densities present in the inner region, could be suppressing the observed recovery fraction (see Figure 1).

Representative differences between the input and output photometry of the entire mosaic field are shown in Figure 3(c). The median and standard deviation of the

⁴ http://physwww.mcmaster.ca/~harris/dolphot_primer.txt

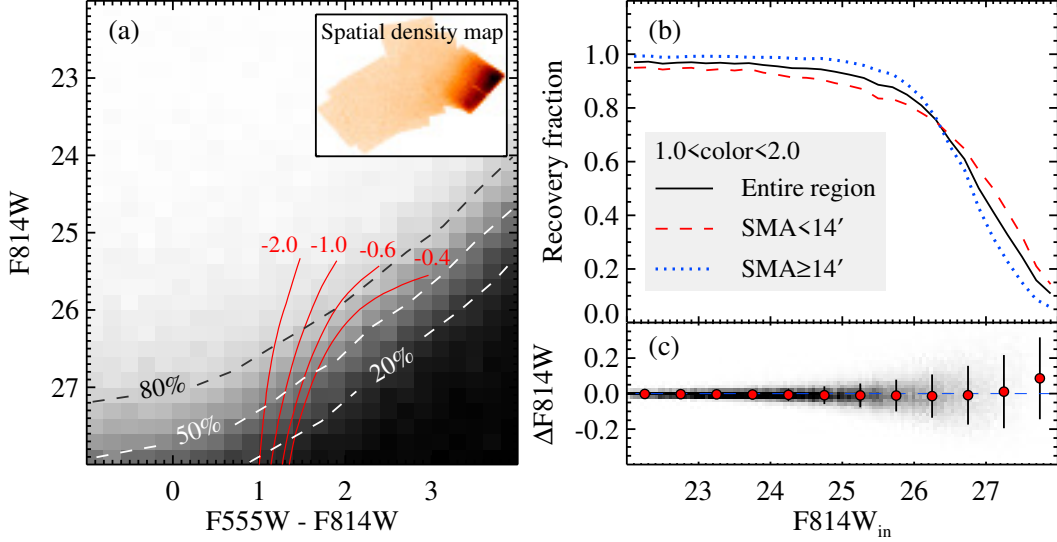


Figure 3. Photometric completeness determined from artificial star tests. (a) Color Magnitude Diagram (CMD) displaying photometric completeness using a color coding from black for fully incomplete (0%) to white (100%) for fully complete. Three representative completeness levels (20%, 50%, and 80%) are shown by dashed lines. Red lines indicate the 10 Gyr isochrones with $[\text{Fe}/\text{H}] = -2.0, -1.0, -0.6$ and -0.4 dex in the Padova model at the distance of NGC 4258 (Bressan et al. 2012). An inset panel displays the spatial density map of the injected artificial stars, which were placed to mimic the true spatial distribution of real stars. (b) Recovery fractions as a function of input F814W magnitude ($F814W_{\text{in}}$) for the stars with $1.0 < F555W - F814W < 2.0$ for the full mosaic and regions interior and exterior to $\text{SMA} = 14'$ (solid, dashed, and dotted lines, respectively). The 50% recovery limit occurs at ~ 27 mag, approximately 1.6 mag fainter than the expected magnitude of the TRGB. (c) The difference between the input and measured magnitudes, $\Delta F814W = F814W_{\text{in}} - F814W_{\text{out}}$, as a function of $F814W_{\text{in}}$ for the full mosaic and stars with $1.0 < F555W - F814W < 2.0$.

difference in input and output magnitudes for artificial stars is given for 0.5 mag bins. The standard deviation, which is an indicator of the true statistical error, ranges from $\sigma_{F814W} \sim 0.01$ mag to ~ 0.14 mag. At the anticipated TRGB magnitude, the photometric dispersion is estimated to be $\sigma_{F814W} = \pm 0.08$ mag, indicating that the quality of our photometry is sufficient to make a high-precision TRGB measurement. Turning our interest to the systematic errors, we also confirm that our photometry is accurate. The median offset between the input and output photometry is only $\Delta F814W \sim 0.01$ mag at the expected TRGB magnitude of $F814W \simeq 25.4$ mag. This is much smaller than the statistical errors at the same magnitude, and also smaller than the typical TRGB detection error in our previous studies ($\sigma_{F814W} \sim \pm 0.04$ mag). Here we emphasize that our TRGB detection technique is based on a series of tests using the artificial stars, so any errors in photometry will be properly incorporated in the final error budget.

2.5. Point Source Selection

The raw DOLPHOT output catalog contains the photometry for various types of objects. Selecting reliable point sources from the raw catalog is important because the inclusion of other types of sources will dilute the

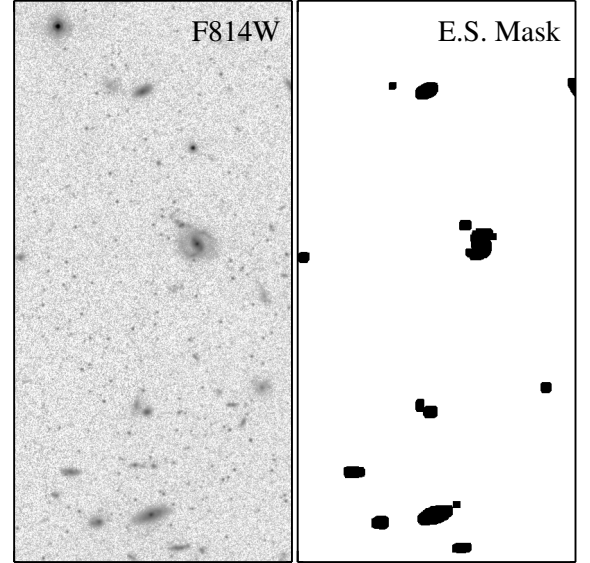


Figure 4. Identification of extended sources. SExtractor was run on the stacked F814W image and a mask of extended sources (either $F814W < 24.5$ mag and class < 0.2 or $F814W < 18.5$ mag and class > 0.8) was created using the segmentation map. Small sections ($10'' \times 20''$) of the stacked drizzled image (left) and the resulting mask map (right) are shown. The DOLPHOT derived sources within the masked black areas were not used any further in the analysis.

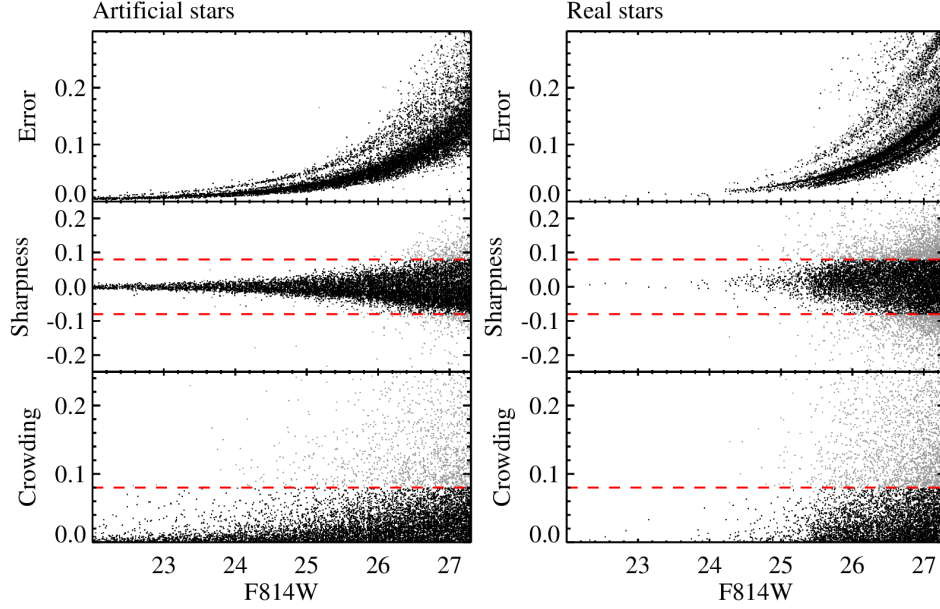


Figure 5. Determination of the point source selection criteria. Distribution of the error (σ_{F814W}) sharpness ($\text{Sharp}_{F814W} + \text{Sharp}_{F555W}$) and crowding ($\text{Crowding}_{F814W} + \text{Crowding}_{F555W}$) parameters as a function of F814W magnitudes are shown. The multiple sequences shown in the error distribution plots (top panels) are the results of the different effective exposure times across the full mosaic. The point-source selection criteria (dashed lines) were based upon the distributions of artificial stars (left) and applied to the observed sources (right). Sources that passed both the sharpness and crowding-based criteria are indicated by black dots.

desired signal coming from the resolved stars. For the aperture correction, we used the *Concentration Index*, C , to select bright point sources, but this process also illustrated how C varied with magnitude, largely showing the parameter to be unreliable across the full catalog. Thus, we select point sources for our TRGB analysis using a more sophisticated series of selection criteria that can be divided into two main steps: 1) using an extended source mask, and 2) using photometric diagnostic parameters (sharpness and crowding). The first step is very efficient in rejecting contaminants in the bright magnitude range, where the sequence of point sources is not clearly defined, while the second step is relatively more important at the faint end. This approach is similar to the method used in the GHOSTS survey (de Jong et al. 2007; Radburn-Smith et al. 2011), which undertook an extensive analysis of the stellar populations in nearby galaxy halos.

To construct the extended source mask, we follow the procedures described in Radburn-Smith et al. (2011). Briefly, we ran SExtractor (Bertin & Arnouts 1996) on the stacked, drizzled F814W image, and obtained a segmentation map with a source catalog. The resulting segmentation map was used to make region masks, identifying intrinsically extended sources ($F814W < 24.5$ mag and $\text{class} < 0.2$), as well as for very bright sources, showing extended halos around their PSF core ($F814W <$

18.5 mag and $\text{class} > 0.8$). The final mask map was constructed after convolving the region mask with a Gaussian filter having a smoothing scale of 3 pixels. The resulting map is shown in Figure 4. Masked regions occupied only 1.5% of the total area of the mosaic field, but, as intended, they reject a significant number of bright extended sources. DOLPHOT-derived sources, falling on the white area of the mask map, were carried forward for the further analysis.

The second step for the point-source selection was made using photometric diagnostic parameters. It is known that the “sharpness” and “crowding” parameters returned from DOLPHOT are useful in selecting point sources (Dalcanton et al. 2009). Our point-source selection criteria are shown in Figure 5. The left three panels show the reported errors, sharpness and crowding values for artificial stars that have the colors of the blue RGB stars, approximately $1.0 < (F555W - F814W) < 2.0$ mag. We used the distributions of these idealized stars as a means of selecting real stars in the observed dataset (seen in the right three panels). Conservative selection criteria were chosen, as shown by dashed lines in the figure. Together with the “sharpness” and “crowding” parameters, we also used $\text{Type} = 1$ (clean stars) sources, and required signal-to-noise ratios higher than

3 in both filters. We provide a summary of the final point-source selection criteria below:

$$|\text{SHARPNESS}_{F555W} + \text{SHARPNESS}_{F814W}| < 0.08, \quad (1)$$

$$\text{CROWDING}_{F555W} + \text{CROWDING}_{F814W} < 0.08, \quad (2)$$

$$S/N_{F555W} > 3.0, \quad S/N_{F814W} > 3.0, \quad \text{and} \quad \text{Type} = 1. \quad (3)$$

Figure 6 presents color-magnitude diagrams (CMDs) of the selected point sources in the 15 ACS pointings. The panels are ordered approximately by their projected distance from the center of NGC 4258 (see Table 1). The shaded cyan-box in each panel of Figure 6 highlights the “blue TRGB” (e.g., that adopted by Jang & Lee 2017; Freedman et al. 2019, among others) and the shaded-region is the same for all panels. From a visual inspection it is clear that the inner fields (i.e., F1 to F6) contain significant numbers of RGB stars spread to either side of the “blue TRGB”, whereas the RGB sequences for the outermost fields (i.e., F12 to F15) are well defined and entirely contained within the “blue TRGB” region. Photometric errors are reasonably small in all the fields, indicating that the observed large spread is not simply a result of the higher stellar density in the inner regions. This is consistent with our assessment that the innermost regions of the mosaic suffer from significant contamination from young, metal-rich stars that populate the outer disk, whereas the outer regions are consistent with being uncrowded and consisting of a primarily old and metal-poor stellar population.

3. PHOTOMETRY VALIDATION CHECKS

In this section, we explore the impact of choices in the photometric processing of our frames on our measurement of the TRGB magnitude in this galaxy. We first examine methodological concerns by comparing two independent sets of stellar photometry, one obtained using DOLPHOT-based routines, the other using DAOPHOT (subsection 3.1). We then examine details of the DOLPHOT reduction, testing three key parameters: Sky Fitting Methods (in subsection 3.2), PSF Size (in subsection 3.3), and PSF Types (in subsection 3.4).

3.1. DOLPHOT vs. DAOPHOT Comparisons

In this section, we compare the photometry from two photometric data-reduction packages. As mentioned earlier, in order to process the complex mosaic

dataset shown in Figure 1, we adopted a DOLPHOT-based methodology unique to this paper, in contrast to the DAOPHOT-based pipeline custom-designed for the CCHP. In the current section we aim to justify this methodology and ensure that any calibration resulting from it can be safely folded into the Freedman et al. (2019) sample.

We select two fields, one in the inner region at $SMA \sim 11'$ (F1) of our mosaic and one in the outer region at $SMA \sim 24.5'$ (F13), as marked by yellow squares in Figure 1, within which we compare the DOLPHOT results with the CCHP pipeline photometry (as described in Beaton et al. 2019). In Figure 7, we show a star-by-star comparison of the two independent photometry sets of the inner (top-left) and outer (top-right) regions. The median offsets at the expected level of the TRGB ($F814W \sim 25.4$ mag) are small: $\Delta F814W = 0.002$ mag in the inner region and $\Delta F814W = 0.023$ mag in the outer region. The error of the median offsets should be larger than 0.014 mag, considering the aperture correction uncertainty of each reduction (0.01 mag). The larger offset in the F13 field is likely due to the shorter exposure time (900s, $S/N \sim 8$ at $F814W \sim 25.4$ mag) than the F1 field (2600s, $S/N \sim 16$ at $F814W \sim 25.4$ mag), together with the larger uncertainty associated with the small number of stars in the TRGB magnitude bin. For example, the F13 field has 85 stars that have a standard deviation of 0.089 mag in the ± 0.25 mag bin of the expected TRGB level. In the same magnitude bin, the F1 field has about 30 times more stars ($N = 2702$) with a smaller standard deviation (0.058 mag). Importantly, because the photometry used for our final TRGB measurement ($SMA \geq 14'$) reached a median effective exposure time of 2736s, we expect the bulk of our photometry to exhibit the same degree of excellent agreement observed in the F1 comparison. This result shows that our two independent pipelines are both reliable and compatible; a TRGB calibration obtained from our DOLPHOT-based reductions can be confidently applied to the TRGB distances measured in Freedman et al. (2019).

In addition to the comparison with the standard CCHP pipeline photometry above, we further investigate the photometry determined from drizzled images. Jang & Lee (2017) independently reduced F1 in the inner region of our mosaic field. They performed point-source photometry using DAOPHOT on the stacked drizzled frames (DRC) using empirical PSFs that were constructed from the same DRC images. We compared our DOLPHOT-based photometry with the photometry used in Jang & Lee (2017) and show the result in the bottom left panel of Figure 7. The bottom right panel

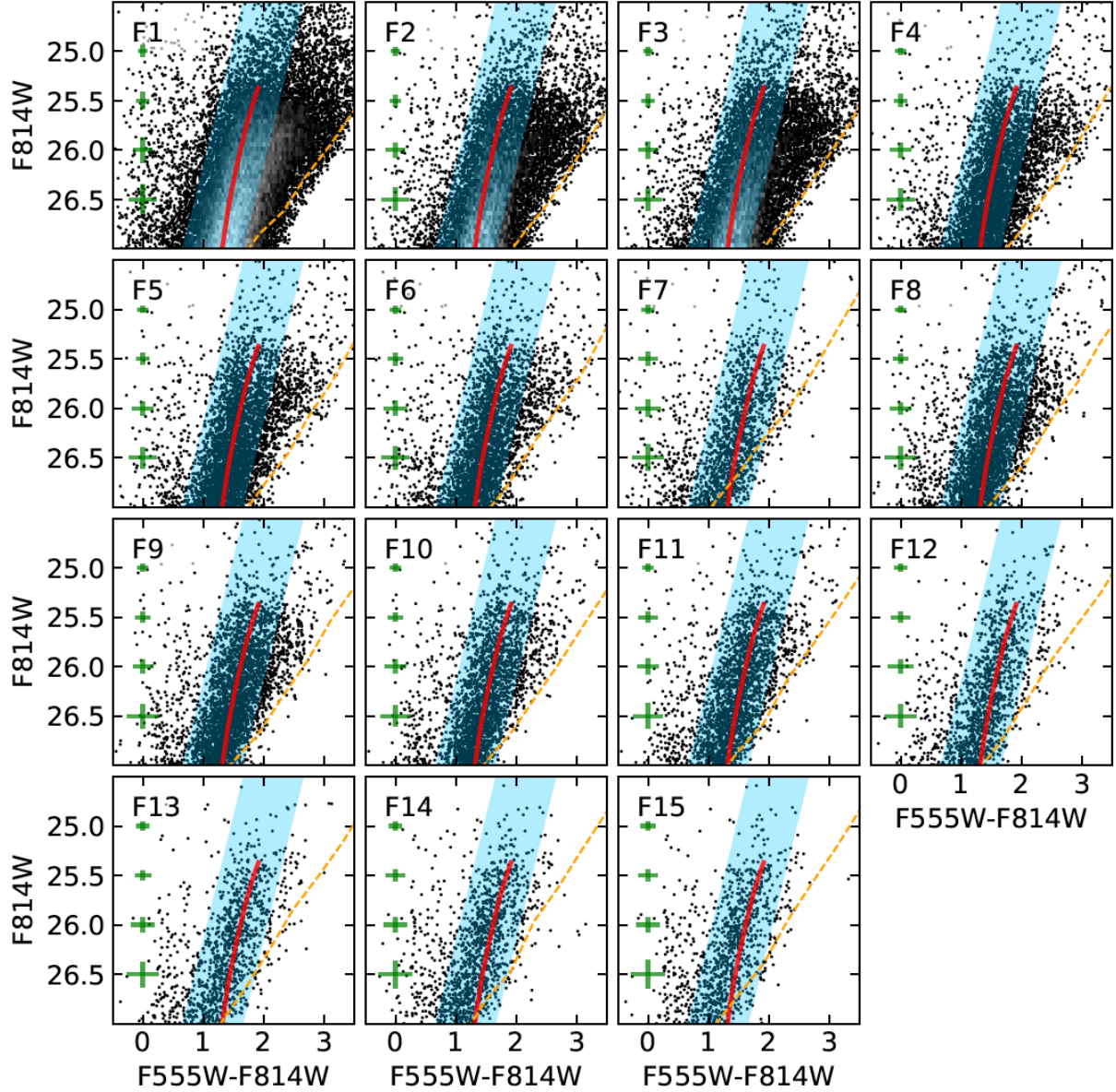


Figure 6. CMDs in F814W versus F555W – F814W for each of the 15 ACS pointings in the mosaic field. The blue shaded region is the same in each panel and represents the “blue TRGB”, which corresponds to the color range where the TRGB absolute magnitude varies little with color. Photometric errors measured at F555W – F814W ~ 1.5 are marked at F555W – F814W = 0. To guide the eye, in each panel a PARSEC stellar isochrone, with an age of 10 Gyr and $[\text{Fe}/\text{H}] = -1.0$ dex, is shown by a solid red line. We shifted the isochrone to the distance modulus $((m - M)_0 = 29.397$ (Reid et al. 2019)) and foreground reddening ($A_{F606W} = 0.040$ and $A_{F814W} = 0.025$ (Schlafly & Finkbeiner 2011)) of NGC 4258. The 50% recovery rate is indicated by a yellow dashed line to the right of the RGB.

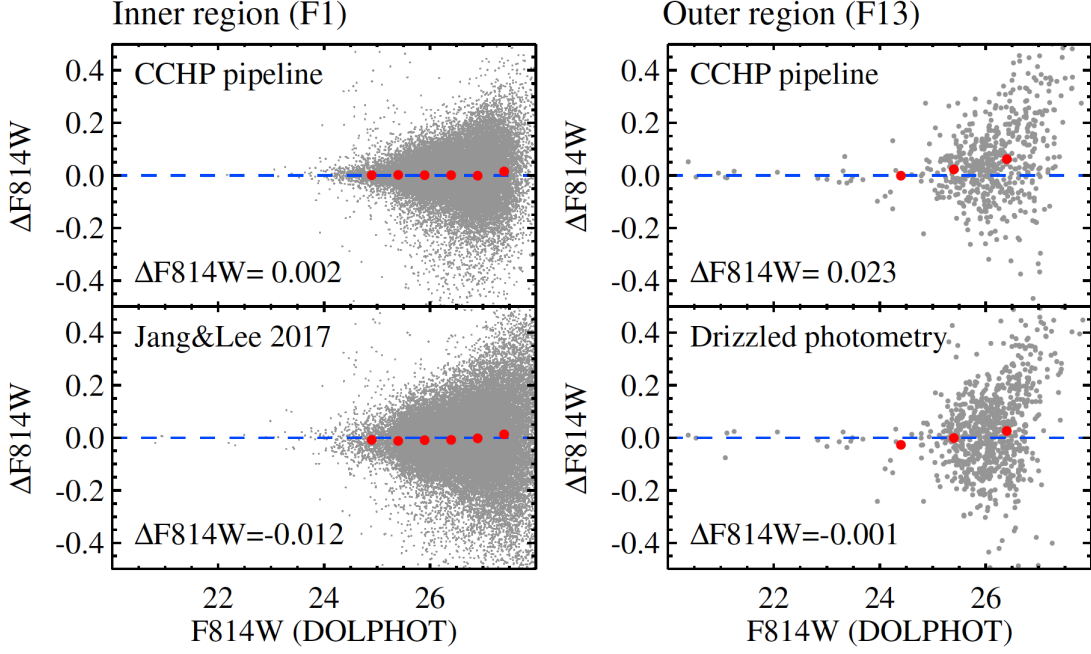


Figure 7. Comparison of photometry between the DOLPHOT and the two DAOPHOT-based reductions. We select two fields in our mosaic dataset: F1 in the inner region at $SMA \sim 11'$ (left panels), and F13 in the outer region at $SMA \sim 24.5'$ (right panels). Comparisons with the CCHP pipeline photometry (DAOPHOT applied to individual FLC frames) are presented in the top. Also shown in the bottom are comparisons with the photometry from drizzled images (DAOPHOT applied to stacked frames using Drizzlepac) from [Jang & Lee \(2017\)](#) (bottom-left) and that produced for this study (bottom-right). Median offsets (defined as DOLPHOT minus DAOPHOT) in each magnitude bin are marked by red dots.

of Figure 7 provides the same comparison for F13. We found that these two independent reductions agree to the 1% level, the median difference at the TRGB magnitude being ~ 0.01 mag.

3.2. Sky Fitting Methods

An accurate measurement of the local sky background is one of the basic requirements for stellar photometry. There are several methods (or algorithms) to measure the local sky, but there is not a singular, universally-adopted algorithm that can meet all scientific goals. In most cases, we chose one of the possible methods based on our prior experiences and proceeded with the data reduction. However, there could be systematic effects in the resulting photometry caused by the method chosen for the sky estimation. We therefore tested our photometry to assess the degree of uncertainty associated with the sky estimation.

There are three representative options in the local sky estimation in DOLPHOT: `Fitsky` = 1, 2, and 3. According to the DOLPHOT manual, the `Fitsky` = 1 option measures the local sky background from an annulus (typically 15 and 35 pixels) prior to the PSF fit. The options `Fitsky` = 2 and 3 are similar; they include the sky level and the PSF model in a two-component fit to the point source profile. Both `Fitsky` = 2 and 3 can be

used for the crowded field photometry, while `Fitsky` = 1 should only be used for very uncrowded regions.

We reduced the mosaic data with all of these above-mentioned sky fitting options. Following the manual, we set `RSky` = 4 10 when the `Fitsky` = 2 option is used. Similarly, we used a small aperture radius of `RAper` = 3 pixels for the `Fitsky` = 1 and 2. Figure 8 displays a comparison of the three reductions. Magnitude differences between the `Fitsky` = 3 and 1 reductions are shown in the top panels, and the same, but with the `Fitsky` = 2 reduction, are shown in the bottom panels. We divided the mosaic field into the inner ($SMA \leq 14'$, left panels) and outer ($SMA > 14'$, right panels) regions to investigate if there is any variation dependent on the stellar crowding.

We found that the three sky fitting options output very similar photometry; in all the cases, the magnitude offsets are almost negligible at the bright side ($F814W \lesssim 24$ mag), and they are only on the order of 0.01 mag at the anticipated level of the TRGB ($F814W \approx 25.4$ mag). Slight differences can be seen in the milli-magnitude level such that the `Fitsky` = 1 reduction appears to provide a better agreement than the `Fitsky` = 2 reduction, as the offsets are ~ 0.005 mag smaller. Similarly, the offsets are smaller in the inner region by ~ 0.015 mag than the outer regions. We note,

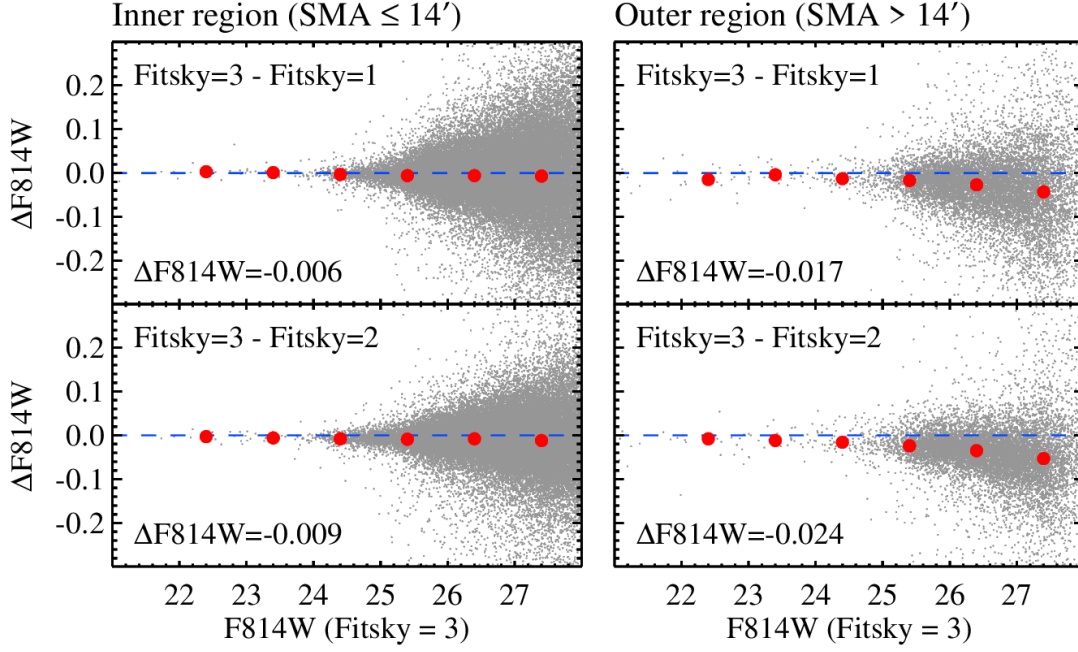


Figure 8. Comparison of photometry determined with different sky fitting options in DOLPHOT (*Fitsky* = 1, 2, and 3). The top panels show magnitude differences between the *Fitsky* = 1 and 3 photometry in the inner (left) and outer (right) regions of the mosaic field. The bottom panels are the same as top panels except for the *Fitsky* = 2 photometry is used for a comparison. Median offsets in each magnitude bin are indicated by red dots. The median offset at the anticipated magnitude of the TRGB is also marked in each panel.

however, that both of the *Fitsky* = 1 and 2 reductions are fainter in all cases than the *Fitsky* = 3 reduction. The photometric accuracy of these reductions can be tested with artificial stars and we provide further details in [Appendix A](#). We found that our main photometry dataset with *Fitsky* = 3 is more accurate than the other two reductions (*Fitsky* = 1 and 2), but there is a slight systematic offset; the recovered magnitudes are fainter than their intrinsic values with $\Delta F814W = 0.01$ mag at $F814W \sim 25.4$ mag (see [Figure A1](#)).

3.3. PSF radius

The parameter *RPSF* determines the size of the PSF radius used for star subtraction. The PSF radius should be sufficiently larger than the full-width at half maximum of the PSF, and thus becomes more important in crowded-field photometry. The DOLPHOT manual recommends the *RPSF* values either of 10 or 13 pixels (depending on the version of the manual; v1.1 to v2.0, respectively); here we test our photometry with both values as is shown in the top panel of [Figure 9](#). We confirmed that the choice of the *RPSF* values, either 10 or 13 pixels, does not meaningfully change the output magnitudes. The median offset at $F814W \sim 25.4$ mag, the vicinity of the TRGB, is only 1 milli-magnitude. The spatial selection does not change the results; both inner

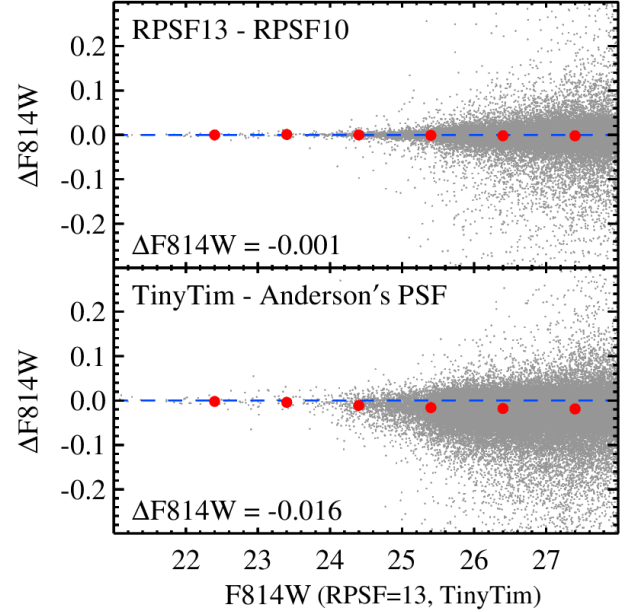


Figure 9. Comparison of PSF fitting choices. The top panel shows the impact of different PSF radii (*RPSF* = 10 and 13 pixels). The bottom panel shows the impact of different PSF models: TinyTim PSF ([Krist et al. 2011](#)) and “Anderson’s PSF” (e.g., [Anderson & King 2006](#)). Median offsets in each magnitude bin are indicated by red dots. The median offsets at the anticipated magnitude of the TRGB are also indicated in the figure.

($SMA \leq 14'$) and outer ($SMA > 14'$) regions show the same offset, $\Delta F814W = -0.001$ mag.

3.4. *TinyTim* versus Anderson’s PSFs

There are two types of PSFs available within DOLPHOT: TinyTim PSFs (Krist et al. 2011) and Jay Anderson’s PSFs (e.g., Anderson & King 2006). While the current version of DOLPHOT does not recommend using the Jay Anderson PSFs due to issues with the implementation of PSF libraries in DOLPHOT, we have tested to see the effects of adopting different PSFs. We found that the choice of PSF types has only a minimal impact; the median difference is negligible at the bright side ($F814W \lesssim 24$ mag) and only $\Delta F814W = -0.016$ mag at the expected magnitude of the TRGB (Figure 9, bottom). The degree of difference is almost the same in the region interior ($\Delta F814W = -0.016$ mag) and exterior ($\Delta F814W = -0.017$ mag) to $SMA = 14'$.

Here we emphasize that all our reductions presented in this paper and all of the reductions used for the CCHP (e.g., Freedman et al. 2019, and references therein) have been carried out using a PSF model determined from the TinyTim PSFs. As a result, PSF-dependent variations are minimized within the CCHP work, but this is a systematic to consider when adopting literature measurements.

3.5. Summary

We summarize here the wide range of stringent photometry comparisons undertaken in this section: different photometry packages (DAOPHOT vs. DOLPHOT), different image types (FLC vs. DRC frames), different local sky fitting methods, and different PSF models (synthetic Tiny-Tim, Anderson’s Core, and empirically measured PSFs). Furthermore, these techniques have also been tested for different levels of stellar crowding (i.e., inner vs. outer regions). From the full range of tests explored in this section, we conclude that an additional systematic uncertainty of 0.02 mag can be added to our final photometry used to measure the TRGB. This conservative estimate of the uncertainty comes mostly from the choice of local sky fitting method, though additional tests explored in Appendix A have shown that our choice of `Fitsky=3` is the most reliable. We included this additional systematic uncertainty in our final error budget in section 6.

4. MEASURING THE TRGB IN NGC 4258

In this section, we present our measurement of the apparent magnitude of the TRGB in the uncrowded, dust-free halo of NGC 4258. Throughout this process, we make decisions that will be explicitly justified in the

sections to follow, and that align with those adopted by the CCHP in prior papers.

We included only those stars with a semi-major axis, galactocentric distance larger than $14'$ (31 kpc). At this extent the mean surface brightness is below $\mu_B \sim 28$ mag arcsec $^{-2}$ (Watkins et al. 2016). The choice to photometer stars in the low-surface-brightness outskirts has several advantages in making a clean determination of the TRGB magnitude. Outside the adopted boundary, the colors of the majority of RGB stars are consistent with them being metal-poor, thus minimizing any trend of the (I -band) TRGB absolute magnitude with color. The RGB stars are also spatially well separated, and the systematic impact from crowding and/or a varying sky background due to unresolved light is thereby minimized. As a result, we see less variation of the observed TRGB magnitude, which indicates that these lines of sight are not passing *through* any extended gas disk of NGC 4258, suggesting that the effect of in situ extinction is minimized as well.

The process for measuring the apparent magnitude of the TRGB is described in Figure 10. We follow the general procedures that were established by Hatt et al. (2017), and refined in later CCHP works. We use the region exterior to $SMA = 14'$ shown in the upper right panel of Figure 1; even with this restriction, a sample of approximately 3,000 stars remains over the $F814W$ one-magnitude range from 25.4 to 26.4 mag. Figure 10(a) and Figure 10(b) show the CMD (black points), the luminosity function (blue), and edge-detection (red) peak response for this selection. The luminosity function (LF) is derived from the stars in the shaded region of the CMD, which has a slope of $\Delta F814W / \Delta (F555W - F814W) = -2.5$ mag with a color boundary of $(F555W - F814W) = 1.3$ and 2.3 mag at the anticipated magnitude of the TRGB. This color-magnitude selection ensures that those sources inconsistent with being blue (metal-poor) RGB stars are not contaminating the marginalized LF. We varied the blue edge of the color cut from $(F555W - F814W) = 1.0$ mag to $(F555W - F814W) = 1.3$ mag and found that the effect on our TRGB detection was less than 0.01 mag. The color-selected LF is finely binned at 0.001 mag, and then smoothed using the GLOESS algorithm with a Gaussian smoothing scale of $\sigma_s = \pm 0.11$ mag. A signal-to-noise weighted Sobel kernel $[-1, 0, 1]$ is applied to the smoothed LF to determine the magnitude where the LF has its greatest change. We detect the apparent magnitude of the TRGB at $F814W = 25.372$ mag.

Our uncertainties are determined as shown in the right three panels of Figure 10. We used a sample of artificial stars that satisfy the color and magnitude bound-

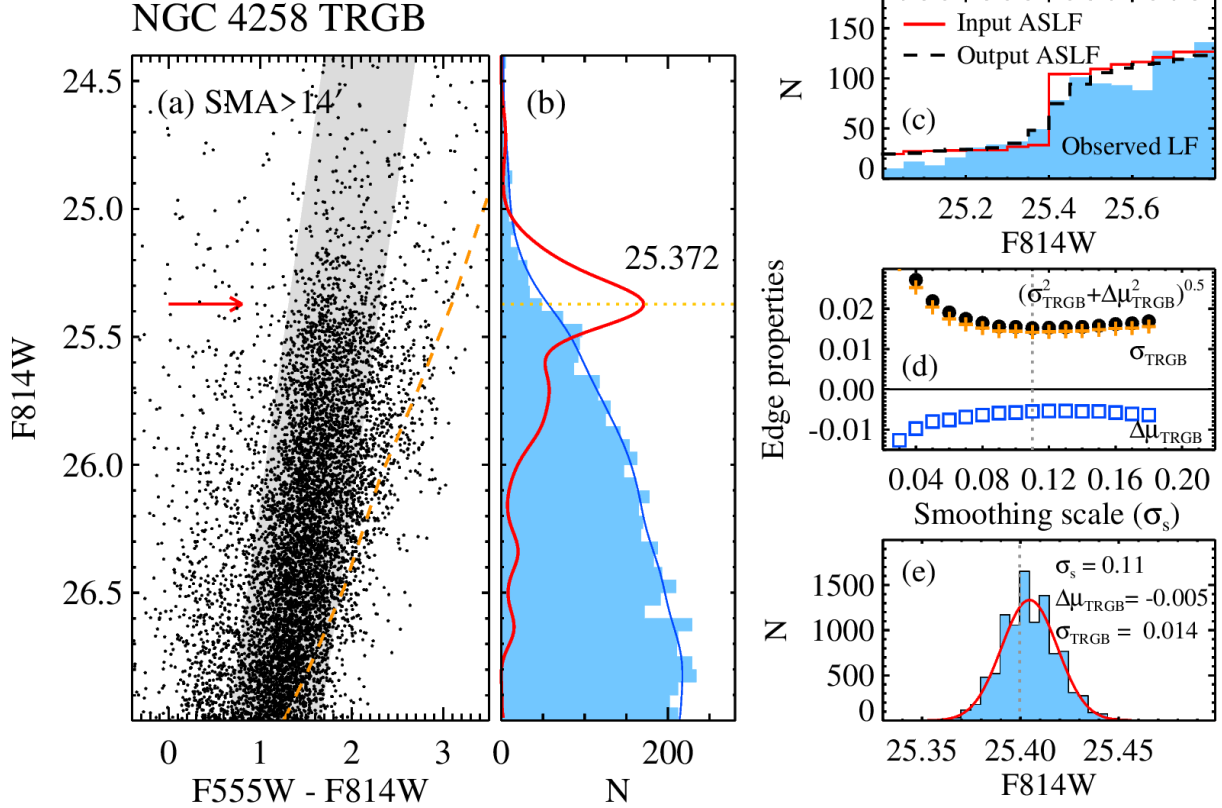


Figure 10. The CCHP determination of the apparent magnitude of the TRGB in NGC 4258. We use only sources more than $SMA = 14'$ from the center of NGC 4258, as shown in Figure 1. (a) CMD of resolved stars beyond $14'$. There are approximately 3000 stars between $F814W = 25.4$ mag and 26.4 mag. A yellow dashed line indicates the 50% completeness level determined from the artificial star tests. (b) Luminosity function (LF) binned at 0.05 mag intervals (blue histogram), also shown as a smoothed curve (blue). Both the LF and the Sobel-edge response (red) were smoothed with $\sigma_s = 0.11$ mag. The smoothed luminosity function is shown by a thin blue line in the middle panel. There is a clear and unambiguous peak in the Sobel edge-detector response at $F814W = 25.372$ mag. (c) Determination of statistical and systematic uncertainties using artificial luminosity functions inserted (red) and recovered (black) from the images. The luminosity function of real stars is shown by a filled histogram for comparison. (d) and (e) Optimization of the smoothing scale and estimation of errors. A quadratic sum of the statistical (σ_{TRGB}) and systematic ($\Delta\mu_{TRGB}$) uncertainties is observed to be minimized when the smoothing scale is set to $\sigma_s = 0.11$ mag. Our analysis suggests $\sigma_{stat} = \sigma_{TRGB} = \pm 0.014$ mag and $\sigma_{sys} = \Delta\mu_{TRGB} = \pm 0.005$ mag.

aries used for the TRGB detection given above. An idealized input luminosity function for the RGB+AGB is generated from artificial stars and its recovered luminosity function is then used for the TRGB detection (Figure 10(c)). Because we know the input TRGB precisely, we can measure any offset from the input value thereby providing a systematic uncertainty, with the scatter about the mean being indicative of the statistical uncertainty. Following Hatt et al. (2017), a series of tests on our artificial luminosity functions have shown that the total TRGB detection uncertainty can be minimized when a Gaussian smoothing scale of $\sigma_s = \pm 0.11$ mag is applied (Figure 10(d)). At this smoothing scale, the statistical and systematic errors are estimated to be $\sigma_{stat} = \pm 0.014$ mag and $\sigma_{sys} = \pm 0.005$ mag (Figure 10(e)). We tested a range of reasonable smoothing scales (large enough to smooth over Poisson noise, but

not too large that the edge is systematically displaced) and find that the effect on the measured TRGB magnitude is 0.01 mag or less.

In summary, for NGC 4258 we have measured the TRGB apparent magnitude for RGB stars in a large region with $SMA > 14'$, giving $F814W_{TRGB} = 25.372$ mag with $\sigma_{stat} = \pm 0.014$ mag and $\sigma_{sys} = \pm 0.005$ mag.

4.1. Variation of the TRGB in the mosaic field

In Appendix B, we discuss the details of optimizing our spatial selection of old and blue (metal-poor) RGB stars. Figure 11 displays CMDs of the mosaic field. The spatial selection is the same as in Figure A2, such that the number of stars in the blue RGB domain (shaded region) is approximately the same from field to field, thereby minimizing sample-size systematics. The edge-detection algorithm applied to the blue

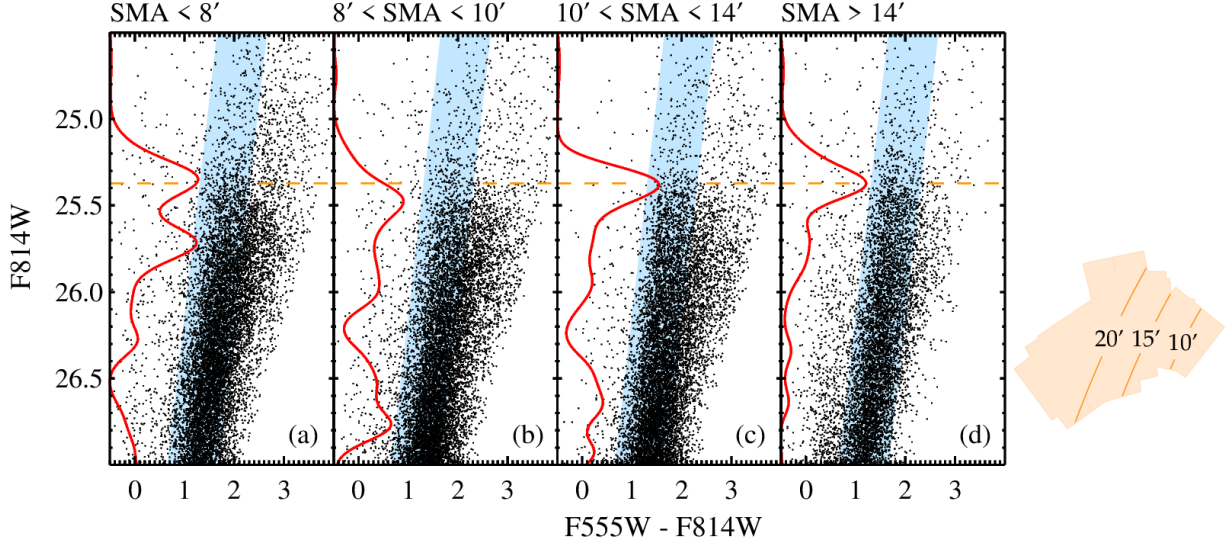


Figure 11. CMDs of resolved stars in four regions of the NGC 4258 mosaic field: $SMA \leq 8'$ (a), $8' < SMA \leq 10'$ (b), $10' < SMA \leq 14'$ (c), and $SMA > 14'$ (d). We selected the blue RGB stars in the shaded region of each CMD and used them for the edge detection (red line). Our optimum detection of the TRGB ($F814W_{\text{TRGB}} = 25.372$ mag) taken from the outer region with $SMA > 14'$ (d) is shown by a dashed line in all panels. A schematic view of the mosaic field is shown on the right.

RGB stars finds maximum responses at (a) $F814W = 25.346 \pm 0.020$ mag, (b) 25.476 ± 0.017 mag, (c) 25.383 ± 0.014 mag, and (d) 25.372 ± 0.016 mag. Here the errors are the quadratic sum of the statistical and systematic uncertainties measured from a series of tests with artificial-star luminosity functions.

It is found that the outer regions with $SMA > 10'$ (Figure 11(c) and Figure 11(d)) have a consistent and stable measurement of the TRGB. There is one prominent peak in the edge detection response at the expected magnitude of the TRGB, where the discontinuity in the luminosity function of the stars in CMDs is clearly seen. The measured TRGB magnitudes are almost identical; indeed the difference between the TRGB detections measured in the outer two fields (0.011 mag) is smaller than their individually quoted 1σ errors (0.015 mag). For the inner two regions with $SMA < 10'$ (Figure 11(a) and Figure 11(b)), we begin to detect slight variations, such that the edge detection responses are fainter (by nearly 0.1 mag) for Figure 11(b), or ambiguous, with two equally-significant peaks seen in Figure 11(a). We suspect that the origin of the unstable measurement is due to the inclusion of disk stars with a possible spread in age and metallicity, together with dust extinction in the plane of the disk, and that these different effects all play a role (see Appendix B). It is well known that for these reasons, the TRGB method is most precise and accurate when applied to stars in the halos of galaxies, and not in their disks.

We next consider optimizing the detection of the TRGB in the mosaic field. Figure 12 shows the variation

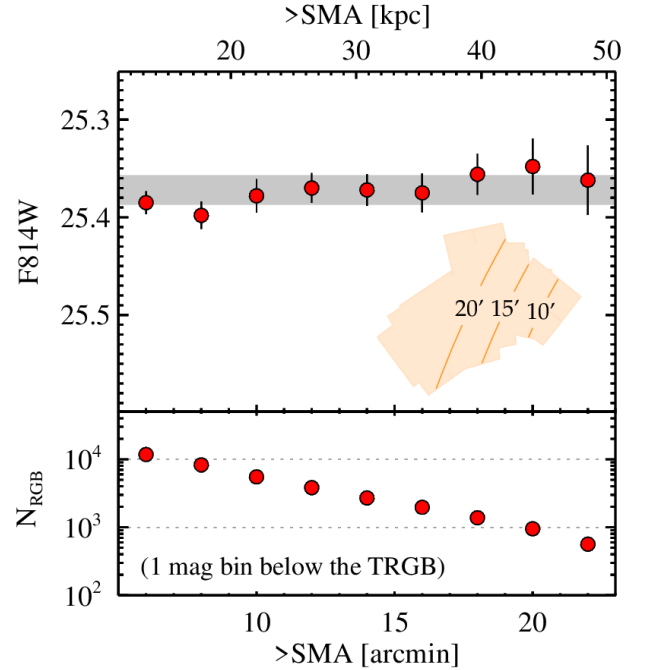


Figure 12. Top Panel: Variation of the measured TRGB magnitude as a function of the SMA. Stars beyond the given radial distance in SMA are used for the TRGB detection. Also shown, inset in the upper panel, is a schematic view of the footprint of the mosaic field with boundaries of three representative radial distances: $SMA = 10', 15',$ and $20'$. Bottom Panel: Number of stars in the one-magnitude bin below the TRGB as a function of SMA.

of the TRGB magnitudes as a function of the spatial selection. The blue RGB stars beyond the given radial

distance are selected and used for the TRGB detection (upper panel). The measurement errors become larger for the outer regions because of the diminishing numbers of stars available to define the TRGB (bottom panel). Nevertheless, the measured TRGB magnitudes appear to be largely consistent over the entire mosaic, but we caution that those measurements including the innermost regions ($SMA \lesssim 10'$) should be considered less reliable due to the unstable nature of the TRGB detections at this radius, as shown in Figure 11. Similarly, the measurements relying only on the outermost regions ($SMA \gtrsim 18'$) have less weight because the lower number of stars involved in the detection, which could induce a bias in the TRGB detection (Madore & Freedman 1995; Madore et al. 2009), if the luminosity function is not being completely filled at the brightest magnitudes. It is not obvious how best to impose a spatial cut for the optimal selection of the TRGB, given that each of the measurements agree well within their 1σ uncertainty, but we estimate that a region with $SMA \gtrsim 14'$ is an optimal choice. Nevertheless, we can see that our detection of the TRGB is very insensitive to the spatial selection, and therefore the systematic uncertainty associated with this choice is negligibly small.

4.2. The TRGB in the “Disk” Field: A Cautionary Tale

In this section, we turn our attention to the measurement of TRGB stars in the high-surface-brightness “Disk” region of NGC 4258. In particular, we illustrate why an unbiased TRGB measurement cannot be made in this field, due to a confluence of reddening, population, and crowding effects. This deep ACS field lies in the southern disk of NGC 4258, shown by a blue square in Figure 1. The pointing was chosen and the observations designed with the intent of discovering of Cepheid variables (Greenhill 2003, PID = 9810). As such, multiple visits were required to discover the variables and determine their periods, mean magnitudes and colors. Total exposure times were 18,400s in F555W and 9,200s in F814W-band; significantly longer than the median exposure time of the mosaic field (2780s in F814W), for example.

The field spans from $SMA = 6'$ to $10'.5$, wherein the B -band surface brightness ranges from $\mu_B \simeq 24$ to 26 mag arcsec $^{-2}$ (Watkins et al. 2016), approximately $3 \sim 4$ mag arcsec $^{-2}$ brighter than the outer region we used for the optimal TRGB detection (see also Figure A3). In addition to their determination of the maser distance to NGC 4258, Reid et al. (2019) undertook a calibration of the TRGB absolute magnitude based on a TRGB measurement in this same Disk field presented

in Macri et al. (2006) (which they call “Outer Disk”). For their calibration, they chose a value of zero for reddening intrinsic to the host galaxy at this position in the disk. More recently, Nataf et al. (2020) make the same assumption in their calibration of the Cepheid Period-Color relation using this field.

We point out that the assumption of zero internal reddening along the line of sight to this Disk field is directly contradicted by Cepheid results previously presented in Macri et al. (2006), who use the exact same Disk dataset. Their uncorrected TRGB magnitude is $I = 25.42 \pm 0.02$ mag. However, through their multi-wavelength analysis of the Cepheid Leavitt Law, these authors found a differential modulus $\mu_V - \mu_I = 0.14 \pm 0.06$ mag. This observed difference in the V and I distance moduli provides direct evidence for some degree of reddening to RGB stars projected into this field.

Indeed, the Cepheid analysis, given in Macri et al. (2006), makes it quite clear that these stars are significantly reddened: they actually measure individual line-of-sight reddenings on a star-by-star basis (as given in their Table 6). In Figure 13 we show histograms of their reddenings determined for Cepheids in both their Inner and Outer disk fields. There is no question that the Cepheids in these fields are reddened and extincted. While the Population II RGB stars are expected to have lower extinction than Cepheids, given the non-zero reddening confirmed across the disk field, it is hard to rule out the possibility that RGB stars projected into the Disk field will not also suffer from extinction. We view the Cepheid reddening values both as an upper limit and as evidence for non-zero reddening to RGB stars in this Disk field.

Adding further evidence in support of the fact that the Disk field is problematic for a measurement of the TRGB, in Figure 14 we present multi-wavelength imaging across the body of NGC 4258: SDSS *gri* (left), GALEX FUV+NUV (middle) and neutral hydrogen column density (right, Heald et al. 2011). The *gri* imaging suggests the presence of blue star-forming regions in the Disk field, which is strengthened by the existence of UV-bright counterparts to these suspected star-forming regions. Both panels strongly suggest that there is a significant population of young and intermediate-aged stars distributed throughout this disk field. Together with the HI column density measurements, we display an example mapping between column density to color excess, from Bohlin et al. (1978). Significant star formation is indicated by the shorter wavelength imaging, in addition to evidence from the ensemble of multi-wavelength data that there exist nonzero quantities of internal dust extinction in and across the lines of sight to this field.

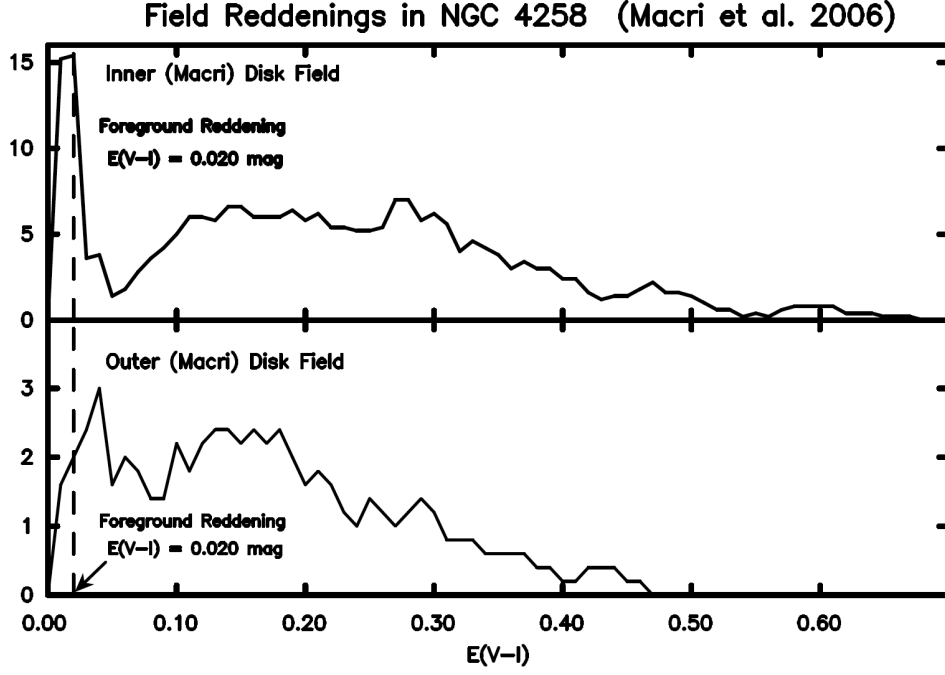


Figure 13. Smoothed histograms of individual Cepheid $E(V - I)$ reddenings in NGC 4258, as published by Macri et al. (2006) for their “Inner Disk” field (upper panel) and their “Outer Disk” field (our Disk field; lower panel). The Milky Way foreground reddening is shown by the dashed vertical line at $E(V - I) = 0.020$ mag. Both fields have considerable reddening: the Inner field has a median reddening of about 0.25 mag, while the Outer field has a median reddening of 0.15 mag in $E(V - I)$.

To further explore the effects of young stellar populations and dust in the Disk field, we turn to comparisons of resolved stellar photometry and edge detection response functions between the Disk field and our adopted halo mosaic selection. In Figure 15 we display CMDs of the inner ($SMA \leq 9'$ of the blue region in the right-most panel) and outer ($SMA > 9'$ of the blue region in the right-most panel) regions of the Disk field (Figure 15(a) and Figure 15(b)). For comparison, Figure 15(c) is a CMD of the halo dominated region ($SMA > 14'$ (the orange region shown in the right-most panel) we used for the optimal detection of the TRGB. Overplotted in red on each CMD is an edge detection response function, computed from stars contained within the blue color-selection region, introduced in the previous section. For reference, the CMD and response function shown in panel (c) are equivalent to those shown in Figure 10 and Figure 11(d). The yellow-dashed line demarcates the TRGB magnitude $F814W = 25.372$ mag, as measured from our adopted mosaic halo dataset.

The inner region of the Disk field (Figure 15a) exhibits clear signs of young and intermediate-aged stellar populations: a Population I (blue) main sequence (the vertical feature at $F555W - F814W \approx 0$) and cooler helium-burning, red supergiants (the slanted feature reaching to $F814W = 23.5$ mag at $F555W - F814W \approx 1.6$). These populations should not be surprising, given that this

disk field was chosen to sample Cepheid variables that are themselves slightly evolved but still young Population I supergiants. A sharp truncation in source counts, which could be seen as evidence for the TRGB, can be seen near $F814W \simeq 25.5$ mag and $F555W - F814W = 2.2$, located almost entirely outside of our color selection region.

A small number of stars belonging to the main sequence and He-burning sequences identified in Figure 15(a), are visible in Figure 15(b) in the outer portion of the Disk field ($SMA > 9'$; see inset). Still, the locus of the RGB is displaced to significantly redder colors than those shown in the halo region of panel (c), again lying almost entirely outside of our color selection. In the absence of a significant population of young and intermediate-aged stars, the remaining explanation would appear to be a combination of metallicity and reddening effects. For reference, a reddening vector with magnitude $A_{F814W} = 0.6$ mag is shown.

The CMD presented in panel (c) of Figure 15 shows those sources located in the outermost region of the mosaic dataset, which we adopted as our halo selection. Comparing to the two Disk CMDs, it is immediately apparent that the RGB stars present in either of the Disk CMDs in panels (a) and (b) do not belong to an old, unreddened, or metal-poor population, as required to make an unbiased measurement of the TRGB.

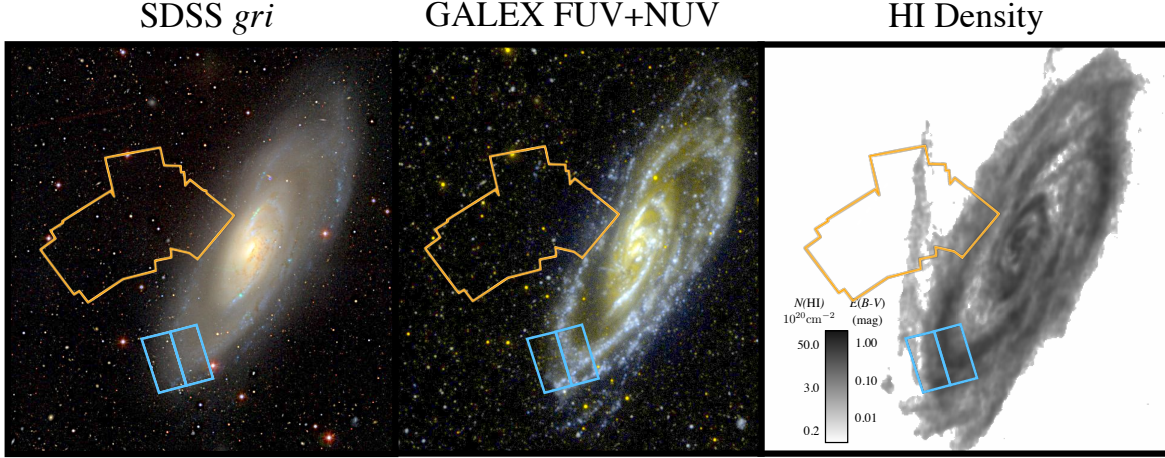


Figure 14. Multi-wavelength diagnostics for NGC 4258: SDSS *gri* color image (left), Galex FUV+NUV color image (middle), and HI Map from Heald et al. (2011) (right). The HI column densities are used to estimate values of $E(B - V)$ based on conversions provided in Bohlin et al. (1978). The halo mosaic field (orange) and Disk field (blue) are overplotted for reference.

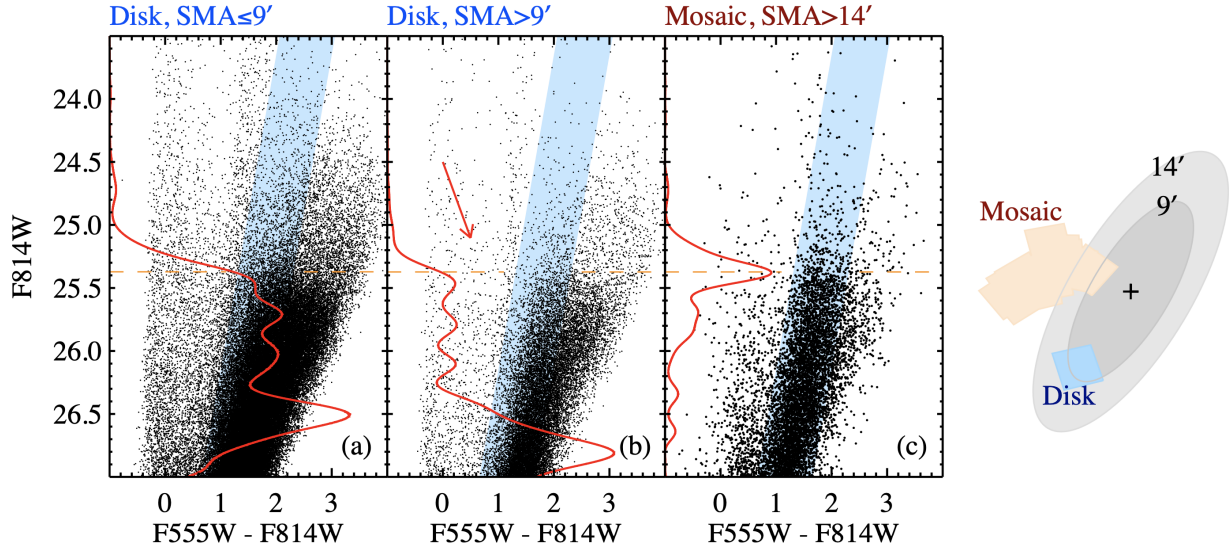


Figure 15. CMDs of the inner ($SMA \leq 9'$) and outer ($SMA > 9'$) regions of the disk field. The third panel shows our CMD of the outer region of the mosaic field ($SMA \geq 14'$), which was selected for the optimum determination of the NGC 4258 TRGB. As in our earlier analysis, we used the blue RGB stars in the shaded regions of the CMDs for the edge detection (red line). An arrow marked in the middle panel (b) shows a reddening vector of $A_I = 0.6$ mag. A schematic view of NGC 4258 and the (colored) footprints of the two fields discussed in this section, are shown to the far right, outside of the panels.

How might the observations described in this section affect empirical measurements of the TRGB in the Disk field? To answer that question, we examine the edge detection response functions, overplotted in red in the CMDs in Figure 15. We first notice that, in stark contrast to the strongly peaked edge detection response we saw in our adopted halo mosaic dataset, reproduced for reference in panel (c), there is no single, clear peak in the response functions shown for the two Disk regions. This multi-peaked structure in the response function could

be the result of several entangled effects: mixed stellar populations, differential extinction, or source crowding. The observable impact of this ambiguous, multi-peaked degeneracy is borne out in the literature: Macri et al. (2006) found a TRGB magnitude $I = 25.42 \pm 0.02$ mag for the Disk field; and in the same Disk field Rizzi et al. (2007) measured a TRGB magnitude of $I = 25.52$ mag. The two differ by 0.1 mag, which is perhaps a better reflection of the uncertainties associated with measuring the TRGB in this Disk dataset.

To test whether our conclusions drawn from the CMDs could be caused by non-physical, systematic offsets in, for example, photometric colors across independent datasets, we repeated our DAOPHOT-DOLPHOT comparison for the Disk field, in a manner identical to that described in Section 3. A star-by-star comparison was carried out, from which we found that the two independent catalogs of stellar photometry agree well. The mean offset is measured to be smaller than $\Delta F814W = 0.01$ mag.

In summary, the tests described above demonstrate that the Disk region is problematic for measurement of the TRGB. First, the multi-wavelength Leavitt Law provides a constraint on the line-of-sight reddening to individual Cepheids (e.g., Freedman 1988; Freedman et al. 2001). We show the results of this analysis in Figure 13 for Cepheids in the Disk field, providing an upper limit and evidence for non-zero reddening to RGB stars located in the same field. Secondly, the maps presented in Figure 14 provide observational evidence of interstellar gas/dust, and recent star formation in the Disk region, suggesting the Disk field suffers from population-mixing effects and reddening. Third, from the CMDs in Figure 15, we showed that there is a clear redward displacement of the RGB locus in the Disk region with respect to that in the Halo selection, potentially suggestive of metallicity or reddening effects, or both. With a wide range of unconstrained astrophysics at play, we conclude that the TRGB cannot be accurately measured in the NGC 4258 Disk field, and that our measurement, which uses the mosaiced halo dataset, provides the current best, unbiased measurement of the Population II TRGB in NGC 4258.

5. COMPARISON WITH OTHER TRGB MEASUREMENTS

In the following, we summarize the previous TRGB measurements in NGC 4258 with a tabulation presented in Table 4. We first describe each of the studies individually, and close by discussing them in aggregate.

In an early study, Mouhcine et al. (2005) reduced a WFPC2 pointing on the minor axis (Ferguson 2001, PID = 9086), which is similar in location to field F1, used in this study. Mouhcine et al. performed aperture photometry to extract the magnitudes and colors of resolved stars. Mouhcine et al. then obtained two measurements of the TRGB, one using a maximum-likelihood based technique and the other using a Sobel edge detector, finding $I_{\text{TRGB}} = 25.25^{+0.13}_{-0.02}$ mag for the former and $I_{\text{TRGB}} = 25.22 \pm 0.09$ mag for the latter. Further discussion of this field is given in Appendix C.

Subsequently Macri et al. (2006) used an ACS pointing into the disk of NGC 4258 situated on the major axis at SMA $\sim 8'$ (Greenhill 2003, PID = 9810), which they call the “Outer Disk” field (our Disk field). This pointing was specifically designed for the discovery of Population I Cepheid variables. Using a Sobel edge detector, they found $I_{\text{TRGB}} = 25.42 \pm 0.02$ mag.

Rizzi et al. (2007) reduced three ACS pointings around NGC 4258: one on the minor axis (Madore 2002, PID = 9477), and two on the major axis, which are the “Inner Disk” and “Outer Disk” fields from Macri et al. (2006). The minor axis field was used for the color-dependent calibration of the TRGB. The two disk fields were used to compare their TRGB distance to NGC 4258 with that from Cepheids in Macri et al. (2006). Rizzi et al. measured the TRGB using a Maximum-Likelihood (ML) luminosity function fitting technique (developed by Makarov et al. 2006) and found $I_{\text{TRGB}} = 25.45$ and 25.52 mag for the Macri et al. “Inner Disk” and “Outer Disk” regions, respectively; they take the average of the two distances for a final result of $I_{\text{TRGB}} = 25.49 \pm 0.05$ mag.

Mager et al. (2008) processed two fields: one taken with ACS (Madore 2002, PID = 9477) and a field at a similar position with WFPC2 (Ferguson 2001, PID = 9086). Both fields were on the minor axis with the intention of avoiding the disk of NGC 4258. They introduced a color-corrected tip magnitude for the TRGB detection defined by Madore et al. (2009) as $T = I_0 - 0.20[(V - I)_0 - 1.5]$. Using a Sobel edge detector, run on the T -band luminosity function they found statistically consistent results from the two fields: $T_{\text{RGB}} = 25.24 \pm 0.04$ mag from the ACS and 25.20 ± 0.06 mag from the WFPC2.

Madore et al. (2009) used the same data processing of the ACS field as in Mager et al. and determined the TRGB in both I and T systems. The reported values are: $I_{\text{TRGB}} = 25.39 \pm 0.11$ mag and $T_{\text{RGB}} = 25.21$ mag, the latter being similar to that of Mager et al. (2008) in the T system. Though, we note the color-coefficients on the T system were different.

Most recently, Jang & Lee (2017) used the ACS field on the minor axis (Madore 2002, PID = 9477), which is identical to the ACS field studied in Mager et al. (2008), Madore et al. (2009), and named F1 in the present paper. They provided two estimates of the TRGB, one in the native F814W system using the stars in the blue color bin ($1.0 \lesssim (F555W - F814W)_0 \lesssim 2.1$), and another one in a modified photometric system similar to T , but using a quadratic form for the

Table 4. Previous TRGB Measurements

Study	Camera	Field	Technique	System	TRGB Mag
Mouhcine et al. (2005)	WFPC2	near F1 ^a	ML	<i>I</i>	25.25 ^{+0.13} _{-0.02}
			Sobel	<i>I</i>	25.22 ± 0.09
Macri et al. (2006)	ACS	Outer Disk ^b	Sobel	<i>I</i>	25.42 ± 0.02
Rizzi et al. (2007)	ACS	Outer Disk ^b	ML	<i>I</i>	25.52
	ACS	Inner Disk ^b	ML	<i>I</i>	25.45
			Mean	<i>I</i>	25.49 ± 0.06
Mager et al. (2008)	ACS	F1 ^c	Sobel	<i>T</i> ^d	25.24 ± 0.04
	WFPC2	near F1 ^a	Sobel	<i>T</i> ^d	25.20 ± 0.06
Madore et al. (2009)	ACS	F1 ^c	Sobel	<i>I</i>	25.39 ± 0.11
			Sobel	<i>T</i> ^d	25.21
Jang & Lee (2017)	ACS	F1 ^c	Sobel	F814W	25.382 ± 0.031
			Sobel	<i>QT</i> ^d	25.370 ± 0.023
Jacobs et al. (2009)	ACS	F1 ^c	ML	F814W	25.43 ± 0.03
				<i>I</i>	25.46 ± 0.03
This Work	ACS	Mosaic ^{c,e}	Sobel	F814W	25.372 ± 0.014 ± 0.039

^a *HST* Program GO-9086, [Ferguson \(2001\)](#)

^b *HST* Program GO-9810, [Greenhill \(2003\)](#)

^c *HST* Program GO-9477, [Madore \(2002\)](#)

^d Corrected for the foreground extinction ($A_I \sim A_{F814W} = 0.025$ mag)

^e *HST* Program Go-10399 [Greenhill \(2004\)](#)

TRGB slope, called QT ⁵, applied to all the stars without any additional, color-based selections. Their uncorrected (apparent) values for the TRGB magnitude are $F814W_{TRGB} = 25.382$ mag, and $QT_{TRGB} = 25.395$ mag. The resulting values (corrected for reddening), adopting a Milky Way extinction of $A_{F814W} = 0.025$ mag ([Schlafly & Finkbeiner 2011](#)), are $F814W_{0,TRGB} = 25.357 \pm 0.031$ mag, and $QT_{TRGB} = 25.370 \pm 0.023$ mag.

We note that the Extra-galactic Distance Database (EDD) ([Jacobs et al. 2009](#)) has a large number of TRGB-based distances, based on homogeneously processed photometry and uniformly-derived TRGB detec-

tions determined with the [Makarov et al. \(2006\)](#) ML fitting method. The team applies the TRGB zero-point calibration of [Rizzi et al. \(2007\)](#) that includes a metallicity correction computed as a function of the mean color of the TRGB; the EDD reports each step in the distance determination. The EDD tip detection for our F1 ACS pointing ([Madore 2002](#), PID = 9477) is $F814W_{TRGB} = 25.43 \pm 0.03$ mag at a mean RGB color of $(F555W - F814W) = 2.12^{+0.04}_{-0.03}$. We note that their mean color is close to the red-edge of our blue RGB selection box.

As can be seen from inspection of [Table 4](#), the TRGB measurements are on four photometric systems: *I*, *T*, F814W, and *QT*, and involve three main fields: a “Disk” ACS field, the inner Halo ACS field (our F1), and the WFPC2 halo field near F1. The different photometric

⁵ $QT = F814W_0 - 0.116(Color - 1.6)^2 + 0.043(Color - 1.6)$, where $Color = (F555W - F814W)_0$

systems used in each study make it difficult to see a true study-to-study variation of the TRGB magnitudes. We therefore selected those measurements in the native $F814W$ or I system with modern ACS data (disk field or F1) and compared them with our outer halo based measurement. We found that these literature TRGB measurements cover a total range of 0.14 mag (25.38 – 25.52 mag) with a mean of 25.43 mag and a standard deviation of 0.05 mag. Our TRGB measurement ($25.372 \pm 0.014 \pm 0.039$ mag) is, therefore, in agreement with most of the other literature TRGB values within the mutual uncertainties.

6. GEOMETRIC CALIBRATION OF THE TRGB ZERO POINT

NGC 4258 is a known host to an H_2O megamaser, which arises from stimulated emission from compact molecular clouds induced by hard radiation from the supermassive black hole about which they orbit. Its proximity (~ 7 Mpc) enables high-precision measurement of the proper motions and radial velocities of each maser using very long baseline interferometric (VLBI) mapping techniques. The orbits of the masers can be well approximated by a Keplerian rotation curve, resulting in an accurate distance to the galaxy (Greenhill et al. 1995; Reid et al. 2019). Our measurement of the NGC 4258 TRGB can be combined with this geometric distance, to provide an absolute calibration of the TRGB luminosity.

We start from our optimal estimation of the NGC 4258 TRGB, $F814W_{TRGB} = 25.372 \pm 0.014$ (statistical) ± 0.005 (systematic) mag, which is based on the blue (metal-poor) RGB stars in the halo regions ($SMA \gtrsim 30$ kpc), where the in situ extinction should be negligible. As in our previous CCHP papers, we consider systematic uncertainties associated with the photometric calibration: 0.02 mag for the ACS photometric zero-point, 0.02 mag for the encircled energy curves for stars cooler than K -type, and 0.01 mag for the aperture correction. In addition to these systematic uncertainties related to the absolute photometric calibration, our detailed technical investigation of the photometry codes (section 3) and TRGB detection process (see section 4) has revealed the following additional systematic terms: a term for the choice of photometry code and PSF modeling of 0.02 mag, a term for the color selection of 0.01 mag, and a term for effects from selection of a single LF smoothing scale of 0.01 mag.

The Milky Way foreground extinction toward NGC 4258 is known to be small, $A_{F814W} = 0.025 \pm 0.016$ mag (Schlafly & Finkbeiner 2011). Here the error is taken from a quadratic sum of half of the extinction ($\sigma_A = 0.013$ mag), and an additional systematic uncer-

tainty ($\sigma_{halo} = 0.01$ mag) based on the large scale statistical analysis of halo reddenings undertaken by Peek et al. (2015). Finally, for NGC 4258 we adopt the most recently published geometric distance and its associated errors, those being $\mu_0 = 29.397 \pm 0.024$ (stat) ± 0.022 (sys) (Reid et al. 2019).

With all of these terms taken into account, we obtain a TRGB zero-point of $M_{F814W}^{TRGB} = -4.050 \pm 0.028$ (stat) ± 0.048 (sys) with a total error of ± 0.056 mag (2.3% in distance). A summary of our revised TRGB zero-point error budget is given in Table 5.

Table 5. Error Budget for NGC 4258 TRGB Calibration

Sources of Uncertainty for	Final	σ_{stat}	σ_{sys}
TRGB Apparent Distance Modulus	Values	(mag)	(mag)
Edge Detection		0.014	0.005
Photometry Choices		...	0.02
Color Selection		...	0.01
Smoothing Selection		...	0.01
STScI ACS F814W ZP		...	0.02
STScI ACS F814W EE Correction		...	0.02
Empirical Aperture Correction		...	0.01
TRGB _{F814W} (apparent)	25.372	0.014	0.039
A_{F814W} (Galactic foreground)	0.025	...	0.016 ^a
TRGB _{F814W} (true)	25.347
NGC 4258 Maser Distance Modulus ^b	29.397	0.024	0.022
M_{F814W}^{TRGB}	-4.050	0.028	0.048

^a Taken to be half of A_{F814W} and including a 0.01 mag component from internal extinction.

^b Reid et al. (2019)

6.1. Discussion

The calibration of the TRGB given in this paper, $M_{F814W}^{TRGB} = -4.050 \pm 0.028$ (stat) ± 0.048 (sys), calibrated by the geometric megamaser distance to NGC 4258, is in excellent agreement with the totally independent calibration of the TRGB from Freedman et al. (2020) using the DEB distance to the LMC, which gives $M_{F814W}^{TRGB} = -4.054 \pm 0.022$ (stat) ± 0.039 (sys).

For completeness, we simply note that our measurement also meets the additional cross-checks against other TRGB calibrations in the Local Group provided in Freedman et al.; specifically, $M_I^{TRGB} = -4.09 \pm 0.03$ (stat) ± 0.05 (sys) based on a DEB geometric distance to the SMC, and $M_I^{TRGB} = -4.056 \pm 0.053$ (stat) ± 0.080 (sys) based on a composite sample of Galactic globular clusters covering a range of metallicities.

Our calibration is also within one sigma of the value reported by Reid et al. (2019), that being $M_{F814W}^{TRGB} = -4.01 \pm 0.04$ mag. Because we used the same maser distance estimate to NGC 4258 as determined by and used in Reid et al. (2019), it can be shown that the +0.04 mag difference in the reported zero-points comes directly from the TRGB magnitude differences: $F814W_0 = 25.385 \pm 0.030$ mag in Reid et al., and $F814W_0 = 25.347 \pm 0.014$ mag this study. The TRGB magnitude adopted by Reid et al. (2019) was, in turn, derived from two previously published studies: (a) Macri et al. (2006), which is based on the Disk field (where $F814W_0 = 25.398 \pm 0.02$ mag), and (b) Jang & Lee (2017) who used Field 1, the innermost portion of the Halo mosaic field (where $F814W_0 = 25.357 \pm 0.031$ mag) (see Figure 1 for the field configurations). These two measurements are systematically +0.05 and +0.01 mag fainter, respectively, than our TRGB measurement, where the differences can be attributed to a combination of astrophysical systematics present in the Disk field (see Section 4.2).

Our TRGB measurement is fully independent of that described in Jang & Lee (2017): (1) We have analyzed the region exterior to $SMA=14'$ not included in their study. (2) We have undertaken a fully independent processing/reduction of the photometry. And (3) We have utilized an independent CCHP edge-detection strategy. We arrive at statistically identical results for our two (present and past) TRGB measurements ($F814W_0 = 25.347 \pm 0.014$ mag in this study and $F814W_0 = 25.357 \pm 0.031$ mag in Jang & Lee (2017)). For a color selection of $(F555W - F814W) < 2.1$ mag, Jang & Lee find a “Blue-TRGB”, absolute magnitude of $M_{F814W}^{TRGB} = -4.030 \pm 0.068$ mag (their Table 6). This value is based on the distance to NGC 4258 in Riess et al. (2016) ($\mu_0 = 29.387 \pm 0.049 \pm 0.029$ mag). Updating this distance to the Reid et al. (2019) value, the Jang & Lee TRGB zero-point becomes $M_{F814W}^{TRGB} = -4.041 \pm 0.049$ mag, which is also consistent with the value in this paper. Jang & Lee (2017) also provide a zero-point of the TRGB based on the LMC as an anchor, giving $M_{F814W}^{TRGB} = -3.96 \pm 0.11$ mag. There are three sources that contribute to their relatively large uncertainty: (a) the TRGB detection ($\sigma = 0.042$ mag), (b) the I -band extinction ($\sigma = 0.07$ mag), and (c) the uncertainty, at that time, in the distance to the LMC ($\sigma = 0.049$ mag). While this zero-point is +0.087 mag fainter than our new determination based on NGC 4258, its large error results in a low-level (0.7σ) statistical difference.

Our determination of the absolute magnitude of the I -band TRGB is -0.081 mag (1.2σ) brighter than a re-

cent determination by Yuan et al. (2019) ($M_{F814W}^{TRGB} = -3.97 \pm 0.046$ mag). There are four elements that are used to construct the Yuan et al. zero-point: 1) the apparent magnitude of the LMC TRGB (taken from Jang & Lee 2017), 2) an accounting for the stellar crowding of the OGLE photometry (Yuan et al. 2019), 3) the I -band extinction towards the LMC (taken from Haschke et al. 2011), and 4) the eclipsing binary distance to the LMC (taken from Pietrzyński et al. 2019). Yuan et al. have shown that the crowding-dependent bias in the OGLE I -band photometry is very small, being on the order of 0.01 mag, even in the disk region. They obtained the LMC TRGB magnitude from Jang & Lee (2017), who provided the TRGB magnitudes in several regions of the LMC. After applying their corrections for stellar crowding and the filter transformation (from I to $F814W$), Yuan et al. derived a mean TRGB magnitude for the LMC, $F814W_0 = 14.507 \pm 0.012$ (stat) ± 0.036 (sys) mag. Here the statistical error is derived from the standard deviation of the eight TRGB values divided by the square root of the degrees of freedom. However, the locations of the eight TRGB regions measured by Jang & Lee (2017) have considerable overlap (see Fig 9 of Jang & Lee (2017)). The TRGB measurements from these regions are thus not statistically independent, which may lead to an underestimate of the uncertainty, if not taken into account.

The systematic error of the LMC TRGB in Yuan et al. (± 0.036 mag) is dominated by the uncertainty they adopted for the line-of-sight extinction (± 0.03 mag). These authors used the extinction map provided by Haschke et al. (2011), who measured the reddening using the mean color of the red clump stars. While the red clump has been used as a reddening indicator, the intrinsic color of the LMC red clump is not currently well constrained, ranging from $(V - I)_0 = 0.84$ to 0.93 mag (Haschke et al. 2011; Górski et al. 2020; Nataf et al. 2020; Skowron et al. 2020). This would suggest that techniques using the red clump to measure reddenings may be subject to a sizable systematic uncertainty. Taking into account these additional uncertainties, and the conclusions drawn in Freedman et al. (2020), we conclude that the Yuan et al. zero-point agrees with ours at the one-sigma level.

Our determination of the I -band TRGB zero-point, $M_{F814W}^{TRGB} = -4.050$ mag, is consistent with the canonical value of $M_{F814W} \sim M_I = -4.05$ mag (Rizzi et al. 2007; Bellazzini et al. 2004; Tammann et al. 2008; Madore et al. 2009); however, our estimated error is now about 50% smaller than previous TRGB calibration errors.

7. SUMMARY

The main objective of this paper has been to establish a highly accurate and precise geometric calibration of the TRGB method directly in the HST F814W “flight magnitude” system. The 15 TRGB calibration fields in NGC 4258 are located in the outer, gas and dust-free halo of the galaxy NGC 4258, which has a measured geometric distance based measurements from the 22 GHz water masers in the accretion disk around its central black hole.

We have undertaken independent DAOPHOT and DOLPHOT analyses, quantifying the uncertainties in our point source photometry. We present a robust detection of the TRGB at $F814W = 25.372 \pm 0.014$ (stat) mag based on over 3,000 stars (within one magnitude of the TRGB) having mean photometric errors of ± 0.06 mag. Applying a Milky Way foreground extinction correction of $A_{F814W} = 0.025$ mag, and subtracting the maser distance modulus gives $M_{F814W}^{TRGB} = -4.050 \pm 0.028$ (stat) ± 0.048 (sys) mag.

Our new, direct-to-HST calibration is completely independent of, and agrees well with, an earlier calibration of (Freedman et al. 2019, 2020), based on a recent geometric DEB distance to the LMC (Pietrzyński et al. 2019). This study resulted in a TRGB calibration of $M_{F814W}^{TRGB} = -4.054 \pm 0.022$ (stat) ± 0.039 (sys) mag. The LMC-based calibration, however, relies on transformations from Riess et al. (2016) to convert observations in ground-based I to the F814W system. The new calibration presented here bypasses those transformations, and their uncertainties, altogether.

With internal consistency established, we can simply average the two independent CCHP calibrations to determine an updated TRGB zero point of $M_{F814W}^{TRGB} = -4.053$ mag, where the total uncertainty is now reduced by $\sim 30\%$ to ± 0.034 mag (or 1.6% in distance). The broader implication, the impact of adding this second geometric anchor to the TRGB distance scale, means that the conclusions reached in Freedman et al. (2019, 2020) are virtually unchanged in their magnitude, while being significantly strengthened in their statistical and systematic certainty.

ACKNOWLEDGMENTS

We thank Peter Stetson for a copy of the DAOPHOT family of programs as well as his helpful interactions on its use for our science case. I.S.J. is grateful to Dr. Roelof. de Jong for helpful discussions on data reduction and stellar populations in nearby galaxies over the past few years.

Support for program #13691 (PI W.L. Freedman) was provided by NASA through a grant from the Space Telescope Science Institute, which is operated by the Association of Universities for Research in Astronomy, Inc., under NASA contract NAS 5-26555. Support for this work was also provided by NASA through Hubble Fellowship grant #51386.01 awarded to R.L.B. by the Space Telescope Science Institute, which is operated by the Association of Universities for Research in Astronomy, Inc., for NASA, under contract NAS 5-26555. M.G.L. is supported by a grant from the National Research Foundation (NRF) of Korea, funded by the Korean Government (NRF-2019R1A2C2084019).

Some of the data presented in this paper were obtained from the Mikulski Archive for Space Telescopes (MAST). STScI is operated by the Association of Universities for Research in Astronomy, Inc., under NASA contract NAS 5-26555.

This research has made use of the NASA/IPAC Extragalactic Database (NED) and the NASA/IPAC Infrared Science Archive (IRSA), both of which are operated by the Jet Propulsion Laboratory, California Institute of Technology, under contract with the National Aeronautics and Space Administration. We also acknowledge the use of the HyperLeda database (<http://leda.univ-lyon1.fr>).

Funding for the Sloan Digital Sky Survey IV has been provided by the Alfred P. Sloan Foundation, the U.S. Department of Energy Office of Science, and the Participating Institutions. SDSS-IV acknowledges support and resources from the Center for High-Performance Computing at the University of Utah. The SDSS web site is www.sdss.org.

SDSS-IV is managed by the Astrophysical Research Consortium for the Participating Institutions of the SDSS Collaboration including the Brazilian Participation Group, the Carnegie Institution for Science, Carnegie Mellon University, the Chilean Participation Group, the French Participation Group, Harvard-Smithsonian Center for Astrophysics, Instituto de Astrofísica de Canarias, The Johns Hopkins University, Kavli Institute for the Physics and Mathematics of the Universe (IPMU) / University of Tokyo, the Korean Participation Group, Lawrence Berkeley National Laboratory, Leibniz Institut für Astrophysik Potsdam (AIP), Max-Planck-Institut für Astronomie (MPIA Heidelberg), Max-Planck-Institut für Astrophysik (MPA Garching), Max-Planck-Institut für Extraterrestrische Physik (MPE), National Astronomical Observatories of China, New Mexico State University, New York University, University of Notre Dame, Observatório Nacional / MCTI, The Ohio State University, Pennsylva-

nia State University, Shanghai Astronomical Observatory, United Kingdom Participation Group, Universidad Nacional Autónoma de México, University of Arizona, University of Colorado Boulder, University of Oxford, University of Portsmouth, University of Utah, University of Virginia, University of Washington, University of Wisconsin, Vanderbilt University, and Yale University.

Some of the figures used in this paper were based on observations made with the NASA Galaxy Evolution Explorer (GALEX), which was operated for NASA by the California Institute of Technology under NASA contract NAS 5-98034.

Finally, we thank the University of Chicago and the Carnegie Institution for Science for their long-term support of our continuing investigation into the expansion rate of the Universe.

Facilities: HST(ACS/WFC)

Software: Astropy (Astropy Collaboration et al. 2013, 2018), DAOPHOT (Stetson 1987), DOLPHOT (Dolphin 2016), Drizzlepac (STSCI Development Team 2012; Hack et al. 2013; Avila et al. 2015), Matplotlib (Hunter 2007), NumPy (van der Walt et al. 2011), SciPy (Jones et al. 2001),

REFERENCES

- Abraham, R. G., & van Dokkum, P. G. 2014, *PASP*, 126, 55, doi: [10.1086/674875](https://doi.org/10.1086/674875)
- Anderson, J., & King, I. R. 2006, PSFs, Photometry, and Astronomy for the ACS/WFC, Instrument Science Report ACS 2006-01
- Astropy Collaboration, Robitaille, T. P., Tollerud, E. J., et al. 2013, *Astronomy & Astrophysics*, 558, A33, doi: [10.1051/0004-6361/201322068](https://doi.org/10.1051/0004-6361/201322068)
- Astropy Collaboration, Price-Whelan, A. M., Sipőcz, B. M., et al. 2018, *The Astronomical Journal*, 156, 123, doi: [10.3847/1538-3881/aabc4f](https://doi.org/10.3847/1538-3881/aabc4f)
- Avila, R. J., Hack, W., Cara, M., et al. 2015, in *Astronomical Society of the Pacific Conference Series*, Vol. 495, *Astronomical Data Analysis Software and Systems XXIV (ADASS XXIV)*, ed. A. R. Taylor & E. Rosolowsky, 281. <https://arxiv.org/abs/1411.5605>
- Beaton, R. L., Seibert, M., Hatt, D., et al. 2019, *ApJ*, 885, 141, doi: [10.3847/1538-4357/ab4263](https://doi.org/10.3847/1538-4357/ab4263)
- Bellazzini, M., Ferraro, F. R., Sollima, A., Pancino, E., & Origlia, L. 2004, *A&A*, 424, 199, doi: [10.1051/0004-6361:20035910](https://doi.org/10.1051/0004-6361:20035910)
- Bertin, E., & Arnouts, S. 1996, *A&AS*, 117, 393, doi: [10.1051/aas:1996164](https://doi.org/10.1051/aas:1996164)
- Bohlin, R. C. 2016, *AJ*, 152, 60, doi: [10.3847/0004-6256/152/3/60](https://doi.org/10.3847/0004-6256/152/3/60)
- Bohlin, R. C., Savage, B. D., & Drake, J. F. 1978, *ApJ*, 224, 132, doi: [10.1086/156357](https://doi.org/10.1086/156357)
- Bressan, A., Marigo, P., Girardi, L., et al. 2012, *MNRAS*, 427, 127, doi: [10.1111/j.1365-2966.2012.21948.x](https://doi.org/10.1111/j.1365-2966.2012.21948.x)
- Chabrier, G. 2003, *PASP*, 115, 763, doi: [10.1086/376392](https://doi.org/10.1086/376392)
- Dalcanton, J. J., Williams, B. F., Seth, A. C., et al. 2009, *ApJS*, 183, 67, doi: [10.1088/0067-0049/183/1/67](https://doi.org/10.1088/0067-0049/183/1/67)
- Dalcanton, J. J., Williams, B. F., Lang, D., et al. 2012, *ApJS*, 200, 18, doi: [10.1088/0067-0049/200/2/18](https://doi.org/10.1088/0067-0049/200/2/18)
- de Jong, R. S., Seth, A. C., Bell, E. F., et al. 2007, in *IAU Symposium*, Vol. 241, *Stellar Populations as Building Blocks of Galaxies*, ed. A. Vazdekis & R. Peletier, 503–504, doi: [10.1017/S1743921307008903](https://doi.org/10.1017/S1743921307008903)
- Deustua, S. E., & Mack, J. 2018, *Comparing the ACS/WFC and WFC3/UVIS Calibration and Photometry*, Space Telescope WFC Instrument Science Report
- Dolphin, A. 2016, *DOLPHOT: Stellar Photometry*. <http://ascl.net/1608.013>
- Dolphin, A. E. 2000, *PASP*, 112, 1383, doi: [10.1086/316630](https://doi.org/10.1086/316630)
- Ferguson, H. 2001, *Investigating the Formation History of Spiral Galaxy Halos*, HST Proposal
- Freedman, W. L. 1988, *ApJ*, 326, 691, doi: [10.1086/166128](https://doi.org/10.1086/166128)
- . 2017, *Nature Astronomy*, 1, 0121, doi: [10.1038/s41550-017-0121](https://doi.org/10.1038/s41550-017-0121)
- Freedman, W. L., & Turner, M. S. 2003, *Reviews of Modern Physics*, 75, 1433, doi: [10.1103/RevModPhys.75.1433](https://doi.org/10.1103/RevModPhys.75.1433)
- Freedman, W. L., Madore, B. F., Gibson, B. K., et al. 2001, *ApJ*, 553, 47, doi: [10.1086/320638](https://doi.org/10.1086/320638)
- Freedman, W. L., Madore, B. F., Hatt, D., et al. 2019, *ApJ*, 882, 34, doi: [10.3847/1538-4357/ab2f73](https://doi.org/10.3847/1538-4357/ab2f73)
- Freedman, W. L., Madore, B. F., Hoyt, T., et al. 2020, *ApJ*, 891, 57, doi: [10.3847/1538-4357/ab7339](https://doi.org/10.3847/1538-4357/ab7339)
- Gonzaga, S., & et al. 2012, *The DrizzlePac Handbook*
- Górski, M., Zgirski, B., Pietrzyński, G., et al. 2020, *ApJ*, 889, 179, doi: [10.3847/1538-4357/ab65ed](https://doi.org/10.3847/1538-4357/ab65ed)
- Greenhill, L. 2003, *Accurate and Robust Calibration of the Extragalactic Distance Scale with the Maser Galaxy NGC4258*, HST Proposal
- . 2004, *Accurate and Robust Calibration of the Extragalactic Distance Scale with the Maser Galaxy NGC4258 II*, HST Proposal
- Greenhill, L. J., Jiang, D. R., Moran, J. M., et al. 1995, *ApJ*, 440, 619, doi: [10.1086/175301](https://doi.org/10.1086/175301)

- Hack, W. J., Dencheva, N., & Fruchter, A. S. 2013, in *Astronomical Society of the Pacific Conference Series*, Vol. 475, *Astronomical Data Analysis Software and Systems XXII*, ed. D. N. Friedel, 49
- Harmesen, B., Monachesi, A., Bell, E. F., et al. 2017, *MNRAS*, 466, 1491, doi: [10.1093/mnras/stw2992](https://doi.org/10.1093/mnras/stw2992)
- Haschke, R., Grebel, E. K., & Duffau, S. 2011, *AJ*, 141, 158, doi: [10.1088/0004-6256/141/5/158](https://doi.org/10.1088/0004-6256/141/5/158)
- Hatt, D., Beaton, R. L., Freedman, W. L., et al. 2017, *ApJ*, 845, 146, doi: [10.3847/1538-4357/aa7f73](https://doi.org/10.3847/1538-4357/aa7f73)
- Hayes, C. R., Majewski, S. R., Hasselquist, S., et al. 2018, *ApJL*, 859, L8, doi: [10.3847/2041-8213/aac38c](https://doi.org/10.3847/2041-8213/aac38c)
- Heald, G., Józsa, G., Serra, P., et al. 2011, *A&A*, 526, A118, doi: [10.1051/0004-6361/201015938](https://doi.org/10.1051/0004-6361/201015938)
- Hoyt, T. J., Freedman, W. L., Madore, B. F., et al. 2019, *ApJ*, 882, 150, doi: [10.3847/1538-4357/ab1f81](https://doi.org/10.3847/1538-4357/ab1f81)
- Hunter, J. D. 2007, *Computing in Science & Engineering*, 9, 90, doi: [10.1109/MCSE.2007.55](https://doi.org/10.1109/MCSE.2007.55)
- Jacobs, B. A., Rizzi, L., Tully, R. B., et al. 2009, *AJ*, 138, 332, doi: [10.1088/0004-6256/138/2/332](https://doi.org/10.1088/0004-6256/138/2/332)
- Jang, I. S., & Lee, M. G. 2017, *ApJ*, 835, 28, doi: [10.3847/1538-4357/835/1/28](https://doi.org/10.3847/1538-4357/835/1/28)
- Jones, E., Oliphant, T., Peterson, P., et al. 2001, *SciPy: Open Source Scientific Tools for Python*. <http://www.scipy.org/>
- Kim, E., Kim, M., Hwang, N., et al. 2011, *MNRAS*, 412, 1881, doi: [10.1111/j.1365-2966.2010.18022.x](https://doi.org/10.1111/j.1365-2966.2010.18022.x)
- Koopmans, L. 2005, *Imaging the mass structure of distant lens galaxies*, HST Proposal
- Krist, J. E., Hook, R. N., & Stoehr, F. 2011, in *Society of Photo-Optical Instrumentation Engineers (SPIE) Conference Series*, Vol. 8127, *Proc. SPIE*, 81270J, doi: [10.1117/12.892762](https://doi.org/10.1117/12.892762)
- Macri, L. M., Stanek, K. Z., Bersier, D., Greenhill, L. J., & Reid, M. J. 2006, *ApJ*, 652, 1133, doi: [10.1086/508530](https://doi.org/10.1086/508530)
- Madore, B. 2002, *TRGB Distance to the Maser Galaxy NGC4258*, HST Proposal
- Madore, B. F., & Freedman, W. L. 1995, *AJ*, 109, 1645, doi: [10.1086/117391](https://doi.org/10.1086/117391)
- Madore, B. F., Mager, V., & Freedman, W. L. 2009, *ApJ*, 690, 389, doi: [10.1088/0004-637X/690/1/389](https://doi.org/10.1088/0004-637X/690/1/389)
- Mager, V. A., Madore, B. F., & Freedman, W. L. 2008, *ApJ*, 689, 721, doi: [10.1086/592563](https://doi.org/10.1086/592563)
- Makarov, D., Makarova, L., Rizzi, L., et al. 2006, *AJ*, 132, 2729, doi: [10.1086/508925](https://doi.org/10.1086/508925)
- Makarov, D., Prugniel, P., Terekhova, N., Courtois, H., & Vauglin, I. 2014, *A&A*, 570, A13, doi: [10.1051/0004-6361/201423496](https://doi.org/10.1051/0004-6361/201423496)
- Merritt, A., van Dokkum, P., Abraham, R., & Zhang, J. 2016, *ApJ*, 830, 62, doi: [10.3847/0004-637X/830/2/62](https://doi.org/10.3847/0004-637X/830/2/62)
- Mouhcine, M., Ferguson, H. C., Rich, R. M., Brown, T. M., & Smith, T. E. 2005, *ApJ*, 633, 810, doi: [10.1086/468177](https://doi.org/10.1086/468177)
- Nataf, D. M., Cassisi, S., Casagrande, L., & Riess, A. G. 2020, *arXiv e-prints*, arXiv:2006.03603. <https://arxiv.org/abs/2006.03603>
- Peek, J. E. G., Ménard, B., & Corrales, L. 2015, *ApJ*, 813, 7, doi: [10.1088/0004-637X/813/1/7](https://doi.org/10.1088/0004-637X/813/1/7)
- Pesce, D. W., Braatz, J. A., Reid, M. J., et al. 2020, *ApJL*, 891, L1, doi: [10.3847/2041-8213/ab75f0](https://doi.org/10.3847/2041-8213/ab75f0)
- Pietrzyński, G., Graczyk, D., Gellenne, A., et al. 2019, *Nature*, 567, 200, doi: [10.1038/s41586-019-0999-4](https://doi.org/10.1038/s41586-019-0999-4)
- Radburn-Smith, D. J., de Jong, R. S., Seth, A. C., et al. 2011, *ApJS*, 195, 18, doi: [10.1088/0067-0049/195/2/18](https://doi.org/10.1088/0067-0049/195/2/18)
- Reid, M. J., Braatz, J. A., Condon, J. J., et al. 2009, *ApJ*, 695, 287, doi: [10.1088/0004-637X/695/1/287](https://doi.org/10.1088/0004-637X/695/1/287)
- Reid, M. J., Pesce, D. W., & Riess, A. G. 2019, *ApJL*, 886, L27, doi: [10.3847/2041-8213/ab552d](https://doi.org/10.3847/2041-8213/ab552d)
- Riess, A. G., Macri, L. M., Hoffmann, S. L., et al. 2016, *ApJ*, 826, 56, doi: [10.3847/0004-637X/826/1/56](https://doi.org/10.3847/0004-637X/826/1/56)
- Rizzi, L., Tully, R. B., Makarov, D., et al. 2007, *ApJ*, 661, 815, doi: [10.1086/516566](https://doi.org/10.1086/516566)
- Sabbi, E., Calzetti, D., Ubeda, L., et al. 2018, *ApJS*, 235, 23, doi: [10.3847/1538-4365/aaa8e5](https://doi.org/10.3847/1538-4365/aaa8e5)
- Salaris, M., & Cassisi, S. 1997, *MNRAS*, 289, 406, doi: [10.1093/mnras/289.2.406](https://doi.org/10.1093/mnras/289.2.406)
- Schlafly, E. F., & Finkbeiner, D. P. 2011, *ApJ*, 737, 103, doi: [10.1088/0004-637X/737/2/103](https://doi.org/10.1088/0004-637X/737/2/103)
- Serenelli, A., Weiss, A., Cassisi, S., Salaris, M., & Pietrinferni, A. 2017, *A&A*, 606, A33, doi: [10.1051/0004-6361/201731004](https://doi.org/10.1051/0004-6361/201731004)
- Skowron, D. M., Skowron, J., Udalski, A., et al. 2020, *arXiv e-prints*, arXiv:2006.02448. <https://arxiv.org/abs/2006.02448>
- Spencer, M., Loebman, S., & Yoachim, P. 2014, *ApJ*, 788, 146, doi: [10.1088/0004-637X/788/2/146](https://doi.org/10.1088/0004-637X/788/2/146)
- Stetson, P. B. 1987, *PASP*, 99, 191, doi: [10.1086/131977](https://doi.org/10.1086/131977)
- STSCI Development Team. 2012, *DrizzlePac: HST Image Software*. <http://ascl.net/1212.011>
- Tammann, G. A., Sandage, A., & Reindl, B. 2008, *ApJ*, 679, 52, doi: [10.1086/529508](https://doi.org/10.1086/529508)
- van der Walt, S., Colbert, S. C., & Varoquaux, G. 2011, *Computing in Science & Engineering*, 13, 22, doi: [10.1109/MCSE.2011.37](https://doi.org/10.1109/MCSE.2011.37)
- Verde, L., Treu, T., & Riess, A. G. 2019, *Nature Astronomy*, 3, 891, doi: [10.1038/s41550-019-0902-0](https://doi.org/10.1038/s41550-019-0902-0)
- Watkins, A. E., Mihos, J. C., & Harding, P. 2016, *ApJ*, 826, 59, doi: [10.3847/0004-637X/826/1/59](https://doi.org/10.3847/0004-637X/826/1/59)
- Yuan, W., Riess, A. G., Macri, L. M., Casertano, S., & Scolnic, D. M. 2019, *ApJ*, 886, 61, doi: [10.3847/1538-4357/ab4bc9](https://doi.org/10.3847/1538-4357/ab4bc9)

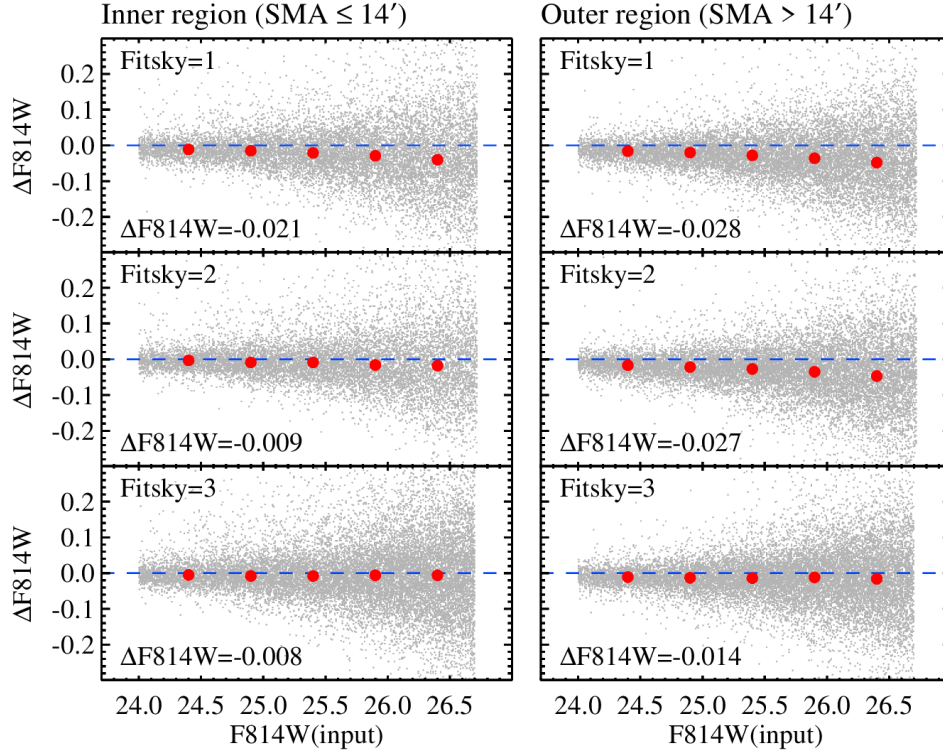


Figure A1. Differences in F814W (inputs minus outputs) vs. input F814W magnitudes for the inner (left) and outer regions (right) with different sky fitting options: *Fitsky* = 1 (top), 2 (middle), and 3 (bottom). The median offset at the TRGB level ($F814W \sim 25.4$ mag) is marked in each panel.

APPENDIX

A. PHOTOMETRIC ACCURACY WITH DIFFERENT SKY FITTING METHODS

Figure A1 displays the results of artificial star tests with the three different sky fitting options (*Fitsky* = 1, 2, and 3) in DOLPHOT. Panels are split into two groups, one for the inner regions ($SMA \leq 14'$, left) and the other one for the outer regions ($SMA > 14'$, right). The input artificial stars have a mean color of $(F555W - F814W) \sim 1.5$, similar to the sequence of the blue RGB stars in the NGC 4258 halo. Red dots show median offsets in each magnitude bin and the offset at the TRGB level is marked in each panel. The error of the median offset is dominated by the statistical error that is estimated to be $\sigma_{\Delta F814W} \simeq 0.002$ mag.

We confirm that the median offsets do not exceed 0.03 mag in all the cases, and they are much smaller than the mean photometric error of ± 0.09 mag at the TRGB level. The offsets are all negative, indicating that the recovered magnitudes are fainter (but only slightly by $0.01 \sim 0.03$ mag) than their intrinsic values. A relative difference is noted such that the *Fitsky* = 3 reduction shows a better agreement with smaller offsets than the other two options (*Fitsky* = 1 and 2). This is consistent with the results from the real star photometry shown in Figure 8; there we found that the *Fitsky* = 1 and 2 reductions are slightly fainter by $0.01 \sim 0.02$ mag than the *Fitsky* = 3 reduction.

This test shows that all the three sky fitting options in DOLPHOT output reliable photometry, but the accuracy can be enhanced when the *Fitsky* = 3 option is used in this dataset. We remind the reader that our main photometry dataset was reduced with *Fitsky* = 3, so that our measurement of the TRGB is based upon the most reliable photometry.

B. OPTIMIZING DETECTION OF THE OLD, BLUE HALO POPULATION FOR TRGB MEASUREMENTS

In Figure A2, we show CMDs of the mosaic field sub-divided into four regions based on the semi-major axis (SMA) radial distance from the center of NGC 4258: (a) $SMA \leq 8'$, (b) $8' < SMA \leq 10'$, (c) $10' < SMA \leq 14'$, and (d)

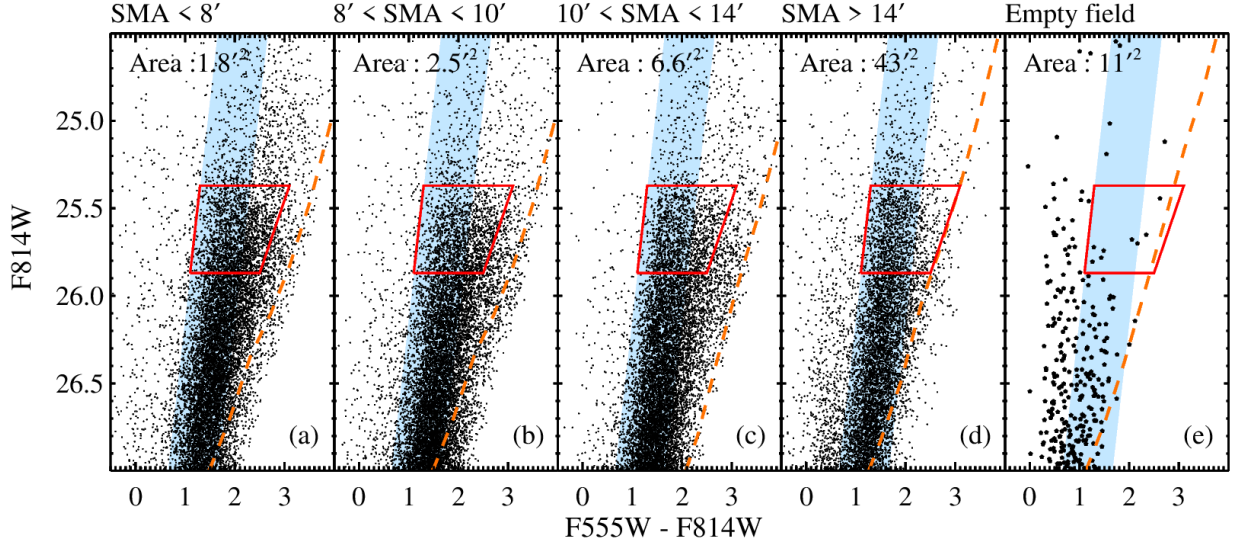


Figure A2. CMDs of resolved stars in the mosaic field of NGC 4258. The panels step out in radial bins in SMA for panels (a) to (d). Panel (e) shows a CMD of a relatively blank field that we used for visualizing the extent of background source contamination, especially in and around the portion of the CMD used to detect and measure the TRGB. Shaded regions represent selection bins for the blue RGB stars. The red polygon denotes the selection region used for the star count profile. The sequence of bright RGB stars (inside the red boxes) narrows and shifts blueward with increasing radius from the center. The outermost bin is dominated by blue (metal-poor) RGB stars. Dashed (orange) lines show the 50% completeness level for each field.

$SMA > 14'$. Each CMD has approximately the same number of stars in the shaded-blue region representing our RGB domain; there are approximately 3,000 RGB stars within one-magnitude fainter than the TRGB in each CMD. The individual field areas are not the same; the outer regions covering wider/larger areas, as annotated at the top of the individual panels. The CMDs of NGC 4258 fields show a gradual change, wherein the sequence of the bright RGB stars near the tip (i.e., stars inside the red box) gets narrower in moving from the inner to the outer regions. The outermost region is dominated and well defined by the blue (metal-poor) RGB stars, similar to the RGB populations in stellar halos of other nearby disk galaxies.

Figure A2(e) shows a CMD of a ‘blank field’ used for the assessment of non-NGC 4258 background sources⁶. The sources in this relatively ‘blank field’ are either foreground stars in the Milky Way or background galaxies that are sufficiently unresolved to pass through our point-source selection filtering (subsection 2.5).

We selected all sources within the red polygon shown in the panels of Figure A2 and plotted their radial star-count profile using filled circles in Figure A3. This profile can be divided into two groups: the blue RGB stars satisfying the color criteria we used for the TRGB detection (those within blue-shaded regions in CMDs and shown by blue circles in Figure A3) and the remaining of the sources that are redder than the blue criteria (red circles). The profiles in Figure A3 are corrected for (a) photometric incompleteness (derived from the artificial star data) and (b) the background contamination from the ‘blank field’ observations (Figure A2(e)). The thick gray line is the B -band integrated light profile of NGC 4258 from Watkins et al. (2016). We took the B -band profile for the east side of NGC 4258 (mean of the green and red lines in Figure 6 of their paper) to get a similar spatial sampling as our RGB counts. The B -band integrated light is scaled to the RGB density using Padova stellar models (Bressan et al. 2012); we generated a well-populated model CMD that has an isochrone-age of 10 Gyr and a metallicity of $[Fe/H] = -1.0$ and assumed a Chabrier initial mass function (Chabrier 2003) from which we derived a relation between the number of RGB stars obeying our selection criteria and its B -band total luminosity. The integrated light profile ends at $SMA \sim 21'$ where the surface brightness reaches $\mu_B \sim 29$ mag arcsec⁻². Beyond this radius, the RGB profiles continues out to

⁶ The position of this field is R.A. = 12:05:45.29, and Decl. = +49:10:53.4, which is about 2.9 deg away from the NGC 4258 center. This ACS field was obtained with a primary aim to study the mass structure of distant lens galaxies (Koopmans 2005, PID = 10494), but it is also useful as background control field for the NGC 4258 fields studied here. Exposure times are F555W in 2320s and F814W in 2388s, similar to the mean depth of the outer regions of the mosaic field.

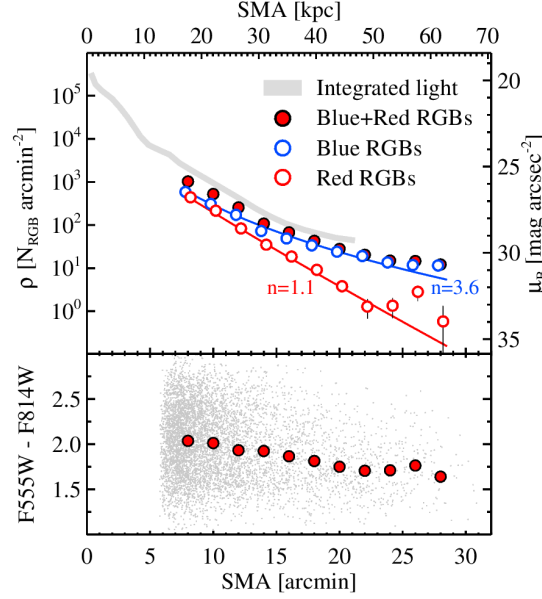


Figure A3. Top Panel: Radial starcount profiles of the blue RGB stars (blue circles), the red RGB stars (red circles), and their sum (filled circles), following the selection polygon in Figure A2. Solid lines represent fitted Sersic profiles for the blue and red RGB density profiles with the parameters specified in the text. The B -band integrated light profile from the minor axis of NGC 4258 in Watkins et al. (2016) is shown by a thick gray line; there is a small systematic offset between this and our RGB starcounts. Bottom Panel: Radial color profile for the RGB stars in the selection polygon from Figure A2. Individual stars and their median color are indicated by grey dots and filled (red) circles, respectively.

$SMA \sim 28'$. There is a slight systematic offset of ~ 0.4 mag between the integrated light and the total RGB counts, which could be due to the presence of the younger stellar populations (mostly AGB stars) as shown in CMDs.

Acknowledging this expected offset, the profiles from the integrated light and total RGB starcount (filled circles) show similar overall trends: the density gradient becomes shallower with increasing radial distance. This transition is mostly due to the blue (metal-poor) RGB population (blue circles), given that the metal-rich RGB stars (red circles) show a more rapid exponential decay with galacto-centric distance.

We fit the blue and red RGB profiles separately with Sersic laws, obtaining Sersic indices of $n_{blueRGB} = 3.6 \pm 1.2$ and $n_{redRGB} = 1.1 \pm 0.2$, respectively. Thus, the blue RGB stars have a spatial distribution similar to other stellar halos, while the red RGB stars follow the disk-like profile. Fitting the blue RGB profile with a power-law results in a power-law index of $\alpha = -3.5 \pm 0.1$ that is consistent with the slope of stellar halos in nearby MW mass disk galaxies ($-5.3 \leq \alpha \leq -2.7$) (Harmsen et al. 2017). Fitting the red RGB profile with an exponential law, we obtain an exponential disk scale length of $h_d = 2'5 \pm 0'1$ (5.5 ± 0.2 kpc), which is similar to the disk scale length of about 6 kpc, as measured by Watkins et al. (2016).

The bottom panel of Figure A3 plots the color of stars from the selection polygon in Figure A2 (grey) against SMA; the median color is computed in radial bins and plotted as filled symbols. A negative color gradient is evident that is related to the population change such that the number of red RGB stars is declining more rapidly than the blue stars. There is no clear boundary between the stellar disk and halo of NGC 4258, but we infer that a region with $SMA \gtrsim 16'$ is a natural point beyond which we reliably sample halo stars; both the B -band integrated light and the total RGB star count profiles start diverging from the extension of the inner disk profile at this radius. For the stars interior to $SMA \gtrsim 16'$ care needs to be taken in recognition of the growing contribution of disk stellar populations. Up to a point, this contribution is, at least, be minimized by judiciously using only the blue RGB stars (e.g., the shaded box in Figure A2).

C. AN INDEPENDENT ANALYSIS OF THE WFPC2 HALO FIELD

There are WFPC2 observations (Ferguson 2001, PID = 9086) taken on the minor axis of NGC 4258, where stellar disk contamination and *in situ* dust extinction are each expected to be low. The exposure times were 11,412s in F606W and 11,700s in F814W, certainly sufficient to detect and measure the resolved RGB population of stars at the distance

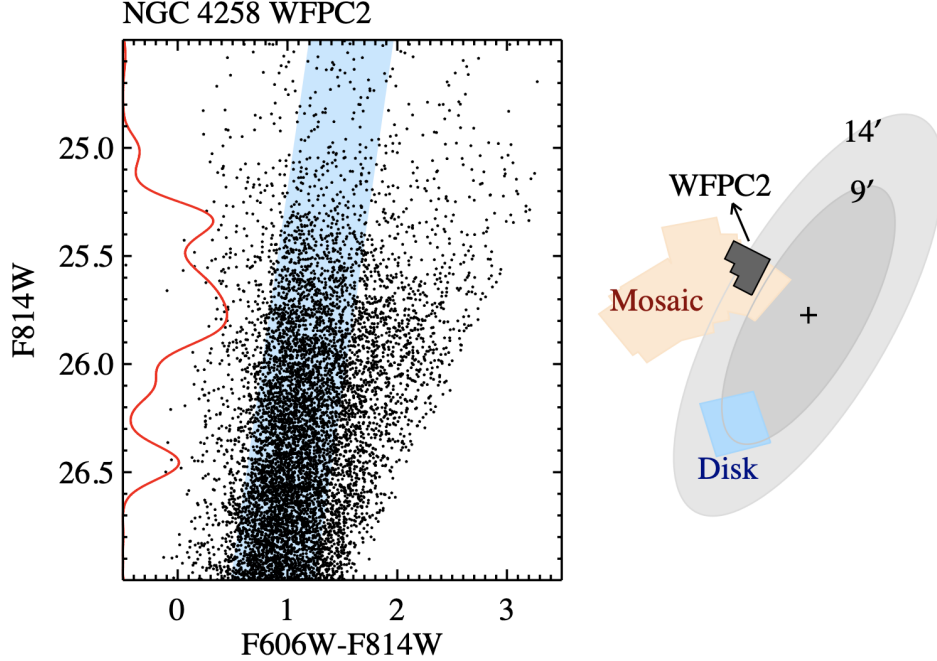


Figure A4. CMD for resolved stars in the WFPC2 field of NGC 4258. The edge-detection filter response (red line) derived from the blue RGB stars (shown in the upward slanting, blue-shaded region) finds a visible peak at $F814W = 25.34 \pm 0.1$ mag, which is identified as the TRGB. Locations of the WFPC2 field (filled black footprint) with respect to the NGC 4258 “Disk” field (blue square) and the mosaic fields (light yellow) are sketched on the right. The filled grey ellipses show the main optical body of the maser-host galaxy NGC 4258.

of NGC 4258. Indeed, this field has been successfully used in two previous studies, each measuring TRGB distances. However, the first study opted to use aperture photometry (Mouhcine et al. 2005) that could have crowding issues. And the second study used the T magnitude system (Mager et al. 2008) for the tip measurement, which is distinct from the $F814W$ magnitude systems used in this work.

We have independently reduced the WFPC2 data and determined the TRGB. We downloaded the science extension (.c0m) of the WFPC2 data and processed them using the DrizzlePac to get a fine alignment solution and better data quality extensions (.c1m). We then used DOLPHOT to derive magnitudes from PSF fitting and leave the magnitudes in the $F814W$ magnitude system. The input parameters we used for the photometry are the same as those in the DOLPHOT/WFPC2 User’s guide. The point source selection was made using the photometric diagnostic parameters: $-0.5 < \text{Sharpness}_{F814W} \leq 0.5$, $S/N_{F606W} > 3.0$, $S/N_{F814W} > 3.0$, and $\text{Type} = 1$.

The CMD of the selected point sources in the three wide field chips is shown in Figure A4. The edge detection algorithm applied to the blue RGB stars (shaded region) finds a peak response at $F814W = 25.34 \pm 0.099$ mag, which we identify with the TRGB. Here the cumulative error is a conservative estimate, derived from the following individual sources: tip detection ($\sigma = 0.05$ mag), aperture correction ($\sigma = 0.05$ mag), and WFPC2 zero-point ($\sigma = 0.07$ mag). This pure WFPC2 data-based measurement is now statistically consistent with our primary result based on the mosaic field, indicating that there is nothing intrinsically flawed with this field or its placement.

We recall from the main text that the prior measurements on this field are $I_{\text{TRGB}} = 25.25^{+0.13}_{-0.02}$ mag and $I_{\text{TRGB}} = 25.22 \pm 0.09$ mag from Mouhcine et al. (2005) and $T_{\text{TRGB}} = 25.20 \pm 0.06$ mag from Mager et al. (2008). The prior results are systematically brighter, but are also likely to be in magnitude systems that are distinct from the native “flight magnitude” system of HST adopted here.